Photoemission spectroscopy using synchrotron radiation. II. The electronic structure of germanium*

W. D. Grobman, D. E. Eastman, and J. L. Freeouf
IBM Thomas J. Watson Research Center, Yorktown Heights, New York 10598
(Received 9 June 1975)

We analyze photoemission spectra for Ge obtained for photon energies $6.5 \leq h\nu \leq 25$ eV and determine the position of energy bands at symmetry points for both filled and empty bands within 1 Ry of the gap. This experimental band structure is obtained using a recently developed anisotropic direct-transition model of photoemission applicable to cleaved single-crystal semiconductors. For the band-structure determination we also employ a direct transition analysis of optical spectra obtained by others. We fit nonlocal-pseudopotential calculations to the experimentally-determined band positions, and thereby determine the importance of both energy and $l = 2$, angular momentum nonlocality in the pseudopotential. Our results for the position of high-lying conduction-band states suggest 0 to +10% self-energy (exchange-correlation) corrections to the energy of electrons excited into the conduction bands. Energy bands which provide a good fit to the experimental band positions are used, along with pseudo-wave-function matrix elements, to calculate various physical properties (photoemission spectra, optical-response functions, and one-electron state densities), and the results of these calculations are compared with experiment. The quality of the fits obtained indicates that the electronic excited-state (and ground-state) properties of Ge for excitations far from the gap are described well by a one-electron model.

I. INTRODUCTION

The electronic band structure of germanium and other covalently bonded semiconductors has been studied extensively for almost two decades using a large variety of experimental tools and theoretical models. Reviews of this work include articles by Phillips,[1] Herman,[2] Cardona,[3] and Cohen and Heine,[4] among others. These reviews and the references therein provide a comprehensive account of the use primarily of optical spectroscopy (including modulation spectroscopy)to determine energy-band separations at various optical critical points in $\vec{k}$ space, as well as indirect fundamental gaps.

Photoemission spectroscopy provides additional information of two types. First, its ability to determine the initial energy of a transition in addition to a valence-band–conduction-band separation provides information about the absolute location of energy bands at different values of $\vec{k}$ relative to the valence-band edge. Second, owing to the different nature[5] of final-state broadening for photoemission compared with optical spectroscopy, and because of its ability to separate the many transitions which occur simultaneously at large $h\nu$, photoemission can give new information concerning high-photon-energy transitions between valence- and conduction-band states which are not evident in conventional optical spectroscopy.[6]

Previous applications of photoemission to the determination of semiconductor electronic structure are of two types. First, there have been relatively low photon-energy [$h\nu \lesssim 6$ eV (quartz optics) or $h\nu \lesssim 11.6$ eV (LiF window cutoff)] measurements of quantum yields and electron energy distributions (for the case of Ge, Refs. 9–11 present representative studies). Second, there have been recent measurements of one-electron density-of-states features of semiconductor valence bands at large values of $h\nu$ using synchotron-radiation light sources,[12–14] He-discharge-lamp radiation[15,16] ($h\nu = 21.2$ or 40.8 eV), and high-resolution x-ray photoemission spectroscopy[16,17] (XPS).

The present paper presents new information on the energy bands of Ge by using photoemission energy distributions obtained over a wider range ($h\nu \leq 25$ eV) than in previous studies, and by interpreting these data using a recently developed anisotropic direct-transition model of photoemission applicable to cleaved semiconductors. Additional experimental data in the form of valence-band overviews, empty-state photoemission spectroscopy,[18] and optical data; and additional theoretical tools including nonlocal-pseudopotential band calculations coupled with a precise $\vec{k}$-space integration technique have enabled us to perform a comprehensive analysis of the energy-band structure of Ge over an energy range of 2 Ry centered on the gap. The resulting experimentally determined band positions are used to study the nature of nonlocal and energy-dependent exchange and correlation effects on the excited electron states, while energy bands which fit well the experimental eigenvalues are used to produce theoretical one-electron state densities, optical response functions, and photoemission spectra, all of which are then compared with experiment.

Previous brief reports of some of this work have appeared in Refs. 19–21.

Section VI, which discusses several physical implications of our analysis, can profitably be read before Secs. II–V, which provide the details of the experimental analysis. Section II describes the experiment, including the different photoemission techniques by which data were obtained, and the manner in which the nature of the information obtained changes depending on the photoemission regime in which the data are taken. Section III discusses the theoretical models employed—the nonlocal-pseudopotential formalism for producing energy bands, and the various $\vec{k}$-space integration formulas relating energy bands, wave functions, and matrix elements to observed quantities. In Sec. IV, overviews of one-electron density-of-states features for both filled and empty states including core levels, valence and conduction bands, and occupied and unoccupied surface states are used to determine different one-electron energy levels, including bulk band positions. Then, in Sec. V, we consider the regime in which photoemission spectra give direct-transition information at general points of the Brillouin zone (BZ). In that section a direct-transition analysis of such spectra is performed in order to identify additional band positions not obtained by density-of-states overviews. Section V also employs a direct-transition analysis of optical spectra obtained by others in order to identify additional band positions. Finally, Sec. VI provides a discussion of the physical significance of the comparison between theory and experiment analyzed in Secs. III–V. The Appendix gives additional details on various aspects of the anisotropic direct-transition model of photoemission not contained in our previous briefer publications.[19,20] This section includes a more detailed comparison of experiment with this model and with the more usual isotropic direct-transition models of photoemission,[22–26] as well as a treatment of light polarization and angle-of-collection effects.

II. PHOTOEMISSION DATA FOR Ge OBTAINED IN DIFFERENT REGIMES

Photoemission data for typical semiconductors can be obtained for any photon energy $h\nu \lesssim 100$ eV using the apparatus employed in the present study.[27] In this apparatus, ultrahigh-vacuum (UHV) cleaved semiconductors are exposed to synchrotron radiation monochromated by either a Seya-type or a specially designed grazing-incidence monochromator. (The latter employs a fixed exit slit and movable entrance slit.) The photon energy bandpass of the monochromators, $\Delta h\nu$, is adjusted by selecting various slit widths.[28] As described in Ref. 28, the energy distribution of the photoelectrons emitted from the sample was measured using a double-pass, electrostatic-deflection cylindrical mirror analyzer. In such an analyzer, one can select emitted electrons of kinetic energy between E^* and $E^* + \Delta E^*$ ($E^* = 0$ corresponds to the vacuum level), where the bandpass ΔE^* is adjustable and is typically ~ 0.1–0.25 eV. Using this apparatus, electron counting techniques are then employed to measure the total flux $F(E^*, h\nu) \times \Delta E^* \Delta h\nu$. Depending on which of the two variables of the experiment are fixed, one can obtain information of two different types.

A. Types of measurements

A *photoemission energy distribution* (PED) results from variation of E^* for fixed $h\nu$, ΔE^*, and $\Delta h\nu$. This is the most commonly employed measuring technique. The processes contributing in this case are illustrated schematically in Fig. 1. The number of electrons emitted at energy E^* is the sum of a *primary* distribution and a *secondary* electron distribution (Fig. 1). The former distribution consists of those electrons which are excited from an initial state of energy E_i (where $E_i = 0$ is defined to be E_v, the valence-band edge, $E_v = E_F$ for Ge), and escape from the solid at energy $E^* = E_i + h\nu - \phi$, where ϕ is the work function. Such primary electrons have lost no energy after being photoexcited. The secondary electrons are those which have suffered at least one inelastic collision before leaving the solid, together with hot electrons excited in the solid by such collisions. As sketched in Fig. 1, the total distribution is cut off near $E^* = 0$ by a surface transmis-

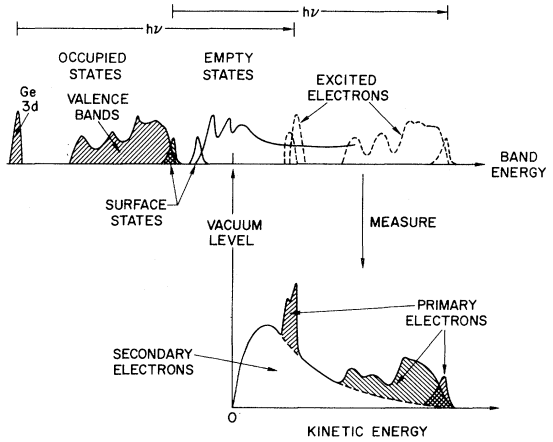

FIG. 1. Schematic illustration of the relation of a photoemission energy distribution (PED) to the occupied density of states. Electrons from occupied states (shaded) are excited upwards by $h\nu$. The fraction escaping without energy loss represents the primary electron distribution, while those created by inelastic scattering are secondary electrons.

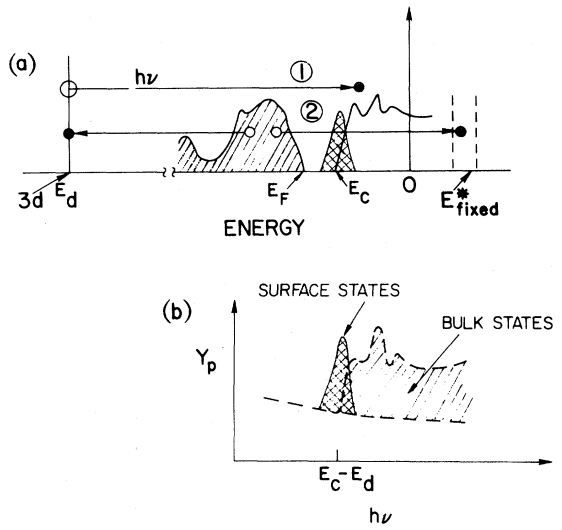

FIG. 2. (a) For $h\nu > E_c - E_d$, $3d$ core holes are created (process 1) at a rate depending on $N_c(E)$, the empty-(surface and conduction band) state density. Such core holes may decay by an Auger process 2, creating electrons at energy E^*_{fixed}. (b) Measurement of intensity at E^*_{fixed} vs $h\nu$ [denoted by $Y_p(h\nu)$], or measurement of the total yield, then reflects features in the density of empty states.

sion function. In this case it is usually the primary electron distribution in which one is interested. Depending on the photoemission regime in which one is working (discussed below), this distribution can contain either both valence- and conduction-band information, or predominately one-electron density-of-states information for the occupied states. In the latter case, one sees prominent features in the occupied bulk and/or surface state (intrinsic or extrinsic) density, modulated by transition probabilities.

In favorable situations one can also obtain information about the *unoccupied* density of states of the conduction bands or surface states by measuring the *partial yield*[29,30] $Y_p(h\nu, E^* = \text{const})$. In such a measurement the kinetic energy E^* is fixed, and is chosen to lie below the energy range in Fig. 1 where valence-band primary electrons are emitted. Y_p is then measured as $h\nu$ is swept through the threshold energy $h\nu_t$ for optical excitation of core electrons (e.g., the $3d$ electrons of Ge) into the empty surface and conduction-band states. $Y_p(h\nu, E^*_{\text{fixed}})$ for $h\nu$ in the vicinity of $h\nu_t$ then contains spectral features (peaks, shoulders, and edges) which reflect one-electron density-of-states features in the empty states.

Figure 2 schematically illustrates the manner in which these results are achieved. Spectral structure of interest in Y_p depends on the successive occurrence of two processes numbered 1 and 2 in Fig. 2. First core holes are created by the excitation of core electrons into the empty states, the rate of creation of such holes depending in part on the number of empty states available. In the second, and independent process, some of these holes decay by creating Auger electrons. A fraction of these escape at the chosen kinetic energy E^*_{fixed}, and others inelastically scatter down to E^*_{fixed} (which is the dominant process). The result is the production of low-energy electrons [shaded area in Fig. 2(b)] in addition to those in the photoemitted distribution due to valence-band photoexcitation. The rate of production of slow electrons versus $h\nu$ then contains spectral features dominated by those contained in the density of empty states.

B. Experimental regimes for measurement of PED's

The measurement of photoemission energy distributions can be described in terms of physical

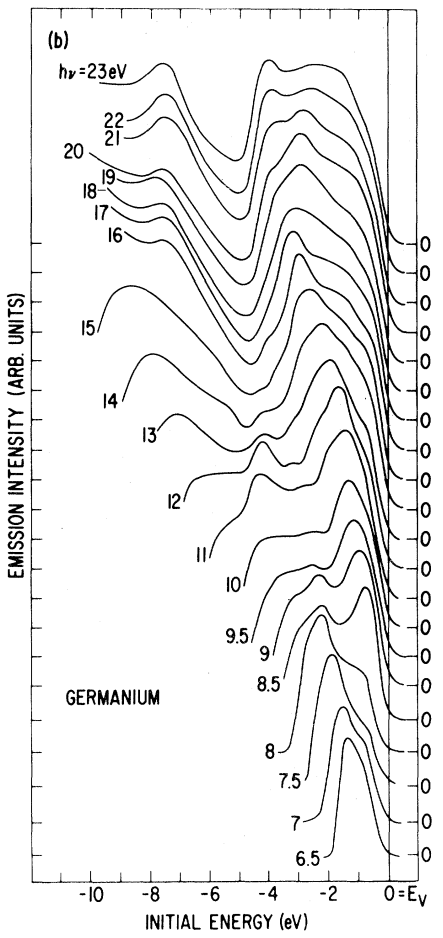

FIG. 3. Valence-band emission intensity vs initial-state energy (PED's) for $6.5 \leq h\nu \leq 23$ eV. Peaks whose initial energy varies as $h\nu$ changes (for $h\nu \lesssim 15$ eV) occur in the "band-structure regime" and contain information about conduction-band dispersion. As $h\nu$ increases above ~20 eV, one-electron density-of-states [$N(E)$] features dominate (see Fig. 8).

regimes[5] determined by the values of $h\nu$ or E^* selected. This is especially important in the case of the present type of study since the wide range of $h\nu$ available spans different regimes. More specifically, when $h\nu$ is large ($\gtrsim$ 25 eV for Ge), one is in the x-ray photoemission spectroscopy (XPS) regime, where one sees features in the one-electron state density of the occupied surface states or of the bulk valence bands [$N(E_i)$ for $E_i \leq 0$]. For $h\nu \lesssim 20$–25 eV in the case of Ge, direct-transition selection rules (crystal momentum $\vec{k}$ conserved in the excitation process) become important, and one sees spectral features whose initial energy E_i changes as $h\nu$ varies, reflecting information about the *joint density* of empty and filled bands (see Sec. III).

The transition between these regimes is illustrated in Figs. 3 and 4, which present angle-averaged PED's obtained on two different cleaved samples in the range $6.5 \leq h\nu \leq 25$ eV. (The reasons for intensity variation of certain spectral features for different samples are discussed in the Appendix C.) As $h\nu$ increases above 20 eV, prominent valence-band features with fixed binding energy (such as the sharp edge at $E_i = -4.5$ eV, or the peak at $E_i = -7.7$ eV) dominate the spectra. On the other hand, spectra in Fig. 3 for $h\nu \lesssim 15$ eV are dominated by peaks whose initial energy values change rapidly as $h\nu$ varies. Finally, the region between approximately $h\nu = 15$ eV and $h\nu = 20$–25 eV is a transition region in which the changing binding-energy (direct-transition) features are becoming weak compared to the one-electron state density features. In this transition region there is a gradual change from behavior typical of the high $h\nu$ "XPS regime" to that typical of the low $h\nu$ "band-structure regime."[5] Analysis of bulk occuped (and unoccupied) electronic density-of-states features obtained in the XPS regime (as well as by partial-yield spectroscopy) will form a large part of Sec. IV, while an analysis of the direct-transition information dominating the band-structure regime is given in Sec. V.

Reference 5 describes these regimes in detail, basing the description on a "Fermi golden rule" formula for photoemission. Such a description is valid for angle-integrated photoemission, in which all emitted electrons are collected. This formula, relevant for the independent-particle description of a solid, gives the current at a detector as

$$R^2 J(\vec{R}, E_i, h\nu) = 2e\left(\frac{e}{2mc}\right)^2\left(\frac{m}{2\pi\hbar^2}\right)^2\left(\frac{2(E_i + h\nu - \phi)}{m}\right)^{1/2} \sum_{\mu \text{ occupied}} \delta(E_i - E_\mu)\left| \int d^3r\, \phi_{\vec{k}}^*(\vec{r}, \hat{R}, E_i + h\nu) \times \Theta(\vec{r})\psi_\mu(\vec{r})\right|^2 . \tag{2.1}$$

Here J is the current from states of initial energy E_i to a detector at position $\vec{R}$ (with $\vec{R} = 0$ on the sample surface), ψ_μ is any occupied bulk or surface state with energy E_μ, Θ is the dipole operator $\frac{1}{2}(\vec{A}\cdot\vec{p} + \vec{p}\cdot\vec{A})$, and $\phi_{\vec{k}}^*$ is the solution to the one-electron Hamiltonian which consists of an *incoming* plane wave along direction $-\hat{R} \equiv -\vec{R}/|\vec{R}|$ at infinite distance from the surface outside of the solid. That is, $\phi_{\vec{k}}^*$ is the usual low-energy-electron-diffraction (LEED) wave function (of energy $E_i + h\nu - \phi$ outside the solid) composed of an incoming plane wave along $-\hat{R}$, matched at the surface to damped Bloch waves inside the solid, and outgoing plane waves (the LEED beams) outside of the solid.

The band-structure regime is obtained if[5]

$$l^{-1}(E) \equiv k_\perp^{(2)} < \delta k_{\text{bands}} , \tag{2.2}$$

where δk_{bands} is a typical $\vec{k}$-space separation (in the direction perpendicular to the surface) between final-state bands of energy $E_i + h\nu$. Inside the crystal, $k_\perp^{(2)}$ is the imaginary part of the Bloch wave propagation vector component perpendicular to the surface. When (2.2) is satisfied, the damp-

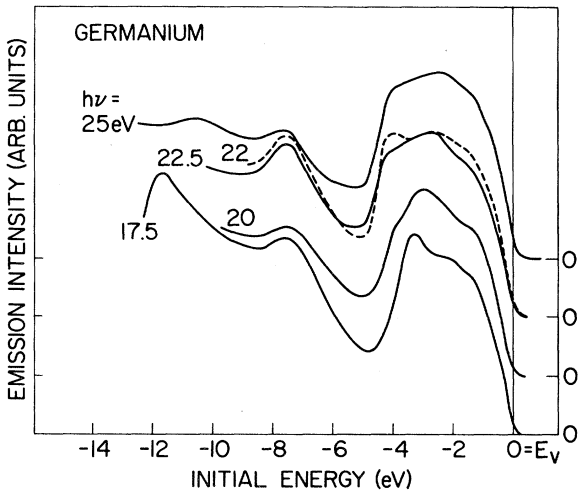

FIG. 4. PED's for $h\nu > 17.5$ eV, mostly in the XPS regime, in which $N(E)$ features dominate. Direct-transitions (moving peak) features are still seen weakly. These spectra are from a different sample than in Fig. 3 and show slightly different intensities for some features due either to sample preparation differences (i.e., cleavage step density) or a different crystal orientation with respect to light polarization (see Appendix, subsection A). Dashed curve is from the sample of Fig. 3.

ing of ϕ_f^* into the crystal is sufficiently small that wave vector $\vec{k}$ is conserved in the optical transition matrix in Eq. (2.1) to better than the separation of the final bands in $\vec{k}$ space. In this case, Ref. 5 demonstrates that direct-transition effects are seen in that portion of $J(\vec{R}, E_i, h\nu)$ coming from initial states ψ_μ which are bulk states (Bloch states matching through the surface to decaying vacuum states).

In addition, there is also a contribution in Eq. (2.1) from initial states ψ_μ which are surface states. In Fig. 3, for example, one sees quite clearly for $h\nu \gtrsim 9$ eV a shoulder at $E_i = -0.7$ eV which is due to surface states, as well as many direct-transition features at lower values of E_i.

When the inequality in Eq. (2.2) is reversed, i.e., when

$$l^{-1}(E) \equiv k_\perp^{(2)} \gg \delta k_{\text{bands}} , \tag{2.3}$$

then the inelastic damping in the solid makes $\vec{k}$ more uncertain than the final-state band spacing in momentum space, and the $\vec{k}$-conservation requirement in the matrix element in Eq. (2.1) does not result in any strong final-state effects. In this XPS regime, most initial states find it possible to make transitions to some final state, and one tends to see predominately one-electron density-of-states features in the primary spectra, although features are still modulated in intensity by transition probabilities.[19] Figures 3 and 4 illustrate that the transition between the band structure and XPS regimes for Ge occurs over a *range* of electron energies, roughly $E_i + h\nu = 15$–20 eV above E_v.

Finally, we will relate the regimes just discussed to the actual values of δk_{bands} and $k_\perp^{(2)}$ for Ge. Few measurements of $l(E)$ for semiconductors have been made, and most of the values quoted are rather unreliable. We have sketched $k_\perp^{(2)} = l^{-1}(E)$ vs $E - E_F$ in Fig. 5, making it a wide band to account for an estimated range of uncertainty in $k^{(2)}$. The lowest energy values (for $E - E_F \lesssim 11.5$ eV) were obtained using Donovan's results[31] for amorphous Ge, which were fit to the total measured yield in the $h\nu \lesssim 11.5$ eV energy range. In this region we also used values for Si obtained in Refs. 32 and 33. For $30 \lesssim E - E_F \lesssim 160$ eV we used results obtained from LEED measurements[33] on Si(100). Above 160 eV, we smoothly joined to the asymptotic behavior for large E, $l(E) \sim E^{-1}$ given by Powell.[34]

A lower-bound approximation to $\delta k_{\text{bands}}(E)$ is given by[35]

$$\delta k_{\text{bands}} \gtrsim k_{\text{BZ}}/n(E) , \tag{2.4}$$

where k_{BZ} is a typical Brillouin-zone radius and $n(E)$ is the number of bands at energy E. Using a spherical-zone empty-lattice model for a fcc Bravais lattice with lattice constant a, we obtain

$$\delta_{\text{bands}} \gtrsim E^{-1} \frac{\hbar^2}{2ma^2} \frac{(2\pi)^3}{3a} \left(\frac{3}{\pi}\right)^{3/2} . \tag{2.5}$$

Plotting the right-hand side of Eq. (2.5) in Fig. 5, we see that the experimental transition region lies in an energy range near the intersection of the curves for $k_\perp^{(2)}$ and the lower bound on δk_{bands}. The position of the transition region is consistent with the fact that the actual value of δk_{bands} lies somewhat above the lower bound in Eq. (2.5).

We may also use Fig. 5 to illustrate the relative importance of surface effects in the spectra. In Fig. 5 we have indicated the wave vector d_{111}^{-1} associated with the ⟨111⟩-direction diamond-structure interlayer separation for Ge ($d_{111} = a\sqrt{3}$) In effect, the line at d_{111}^{-1} in Fig. 5 separates two further regimes (again as a rather ill-defined boundary). The case where

$$k_\perp^{(2)} \gg d_{111}^{-1} \quad \text{and} \quad l(E) \ll d_{111}^{-1} \tag{2.6}$$

correspond to a *surface-dominated* portion of the XPS energy regime. In this region, the ratio of surface-state to bulk emission is enhanced. Also, in this case the momentum uncertainty is comparable to the BZ radius, and $\vec{k}$ is not a good quantum number. Nevertheless, the one-electron density of states of the bulk may still be seen. Equation (2.1) indicates that if ϕ_f^* penetrates at all into the bulk (even for a distance less than d_{111}), then it couples to ψ_μ, which are bulk Bloch states, since such states have finite amplitude at the

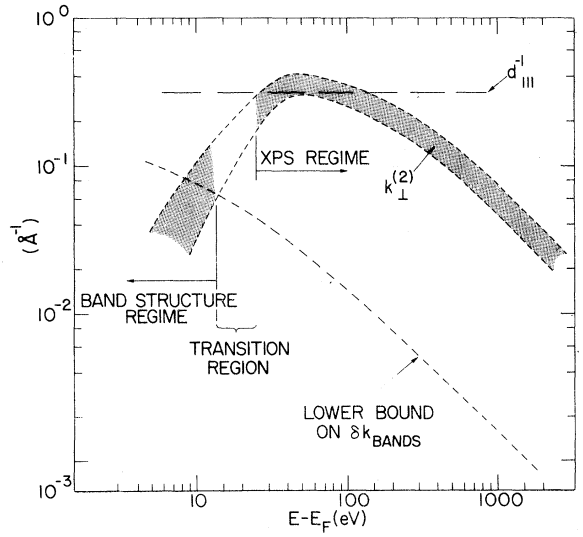

FIG. 5. Imaginary part of the final-state wave vector ($k_\perp^{(2)}$) and lower bound on the spacing between final-state bands in momentum space (δk_{bands}) vs final-state energy E.

surface. As these states are distributed in energy according to the one-electron density of states, one may see one-electron density-of-states features of the bulk. One requirement is that the coherence length of the *hole* state (of the ψ_μ) be large compared with d_{111}. However, there are cases where, in this surface-dominated regime, the bulk density of states may be severely distorted.[36] For $k_\perp^{(2)} \ll d_{111}^{-1}$, one is in a *bulk-dominated* portion of the XPS regime, where $\vec{k}$ is defined to much better than k_{BZ} (i.e., direct transitions occur), but direct-transition effects are not evident since $k_\perp^{(2)} \gg \delta k_{\text{bands}}$. Referring to Fig. 5, we see that this is the case, for example, in EPS measurements at 1486.6 eV which use the Al $K\alpha$ emission line as a light source.

Finally, we note that if Eq. (2.2) holds so that the band-structure regime is achieved, then no over-all surface domination can occur. This is so because Eq. (2.2) automatically implies that $k_\perp^{(2)} \ll d_{111}^{-1}$. Also, Ref. 5 demonstrates that in this case the photoemission current can be written in terms of a direct-transition, "three-step model" of photoemission. Such a model of photoemission, due to many authors (see Ref. 20 in Ref. 5), has been widely used since the work of Berglund and Spicer[22] appeared.

III. THEORETICAL MODELS

The determination of the electronic structure of Ge will proceed in the following sections by interpreting data through the use of several theoretical models which are described in the present section. These models include a bulk energy-band calculation technique as well as formulas by which photoemission and optical properties can be related to the band structure.

A. Nonlocal-pseudopotential model

The pseudopotential technique[4] has been widely used to determine semiconductor electronic structure from optical[1] and photoemission[31,19-21] experiments. We use such a technique here, and in particular we incorporate two types of nonlocality in the pseudopotential. Angular momentum nonlocality, in the form of an $l=2$ repulsive potential, is needed to obtain the proper band topology.[19,37] Physically, it arises from the proximity (in energy) of the Ge $3d$ core levels (see Sec. IV) to the valence and conduction bands.[38] Energy nonlocality may aid in obtaining conduction and valence bandwidths in better agreement with experiment.[19,20] Such nonlocality can become important for describing data relating to optical transitions over a wide energy range, since the energy dependence of the electron self-energy operator becomes significant, as has been shown to be the case for Cu.[24] Such an energy dependence can arise, for example, from the dependence of the correlation energy[39] of optically produced quasiparticles on their energy separation from the Fermi energy E_F. (Such energy dependence is also contained in the pseudopotential itself.[4])

From these considerations we arrive at the following form for the pseudopotential equation used to determine Bloch eigenvalues $E_n(\vec{k})$ [where n is a band index and $\vec{k}$ is a wave vector in the first Brillouin zone (BZ)]:

$$H\psi_{n\vec{k}}(\vec{r}) = [T + v_L + v_2 + \alpha E_n(\vec{k})]\Psi_{n,\vec{k}}(\vec{r}) ,$$
$$= E_n(\vec{k})\psi_{n,\vec{k}}(\vec{r}) , \qquad (3.1)$$

where $\psi_{n,\vec{k}}$ is the pseudo-wave-function. Here T and v_L are the usual kinetic-energy operator and local pseudopotential,[4] v_2 is an angular-momentum-dependent ($l=2$) potential in the form of a repulsive square well,[37,38] and α (>0) is the coefficient of the linear energy-dependent correction to the electron self-energy.[19]

As usual,[4,40] v_L is defined in terms of a reciprocal-lattice-vector Fourier expansion by

$$v_L(\vec{r}) = \sum_{\vec{G}} V(\vec{G})\, e^{i\vec{G}\cdot\vec{r}} , \qquad (3.2)$$

and we keep only $V(\vec{G})$ for $|\vec{G}|^2 = 3$, 8, or 11 in units of $(2\pi/a)^2$, where a is the lattice constant[40] of 5.66 Å. These three Fourier coefficients are then denoted $V(3)$, $V(8)$, and $V(11)$, respectively.

Following Refs. 37 and 38, we use an angular-momentum-dependent[41] potential of the form

$$v_2 = A_2 f(\vec{r}) P_{l=2} , \qquad (3.3)$$

where $P_{l=2}$ is an $l=2$ projection operator, A_2 is the strength (in Ry) of the repulsive square well, and

$$f(\vec{r}) = \begin{cases} 1 & |\vec{r}| \le R_2 \\ 0 & |\vec{r}| > R_2 , \end{cases} \qquad (3.4)$$

where R_2 is the well radius in Å and $\vec{r}=0$ is an ionic position in the crystal. A slightly different form for v_2, using a Gaussian potential, has also been utilized recently[42] in the analysis of optical data. The eigenvalues in (3.1) are found by diagonalizing a matrix consisting of plane-wave matrix elements of the Hamiltonian H. Such matrix elements for v_2 in Eqs. (3.3) and (3.4) are given explicitly in Ref. 37.

In order to find the eigenstates in Eq. (3.1), it is useful to remove the eigenvalue dependence of H. We have done this by using the fact that we will always use $\alpha \ll 1$. In this case the Schrödinger equation can be written

$$(1+\alpha)(T + v_L + v_2)\psi_{n,\vec{k}} = E_{n,\vec{k}}\psi_{n,\vec{k}} , \quad \alpha \ll 1. \qquad (3.5)$$

While Eq. (3.5) can be interpreted as a pseudopotential problem with an "effective mass" $m^* = m_0$

$\times(1+\alpha)^{-1}$, we prefer to view it simply as a transformed version of (3.1) which is computationally more convenient. Indeed, addition of an effective mass in the local-pseudopotential problem has been previously used as a device to change bandwidths in a manner in which the local pseudopotential alone cannot.[2,19,43] Equation (3.1) represents this effect in a form which is more transparently due to the energy dependence of the electron self-energy or of the pseudopotential itself.

B. Calculation of experimental properties

Once energy eigenvalues and wave functions are obtained on a mesh of $\vec{k}$ points in the BZ [by diagonalizing (3.5)], we can determine the optical constants, one-electron density of states, and photoemission spectra by appropriate numerical $\vec{k}$-space integration. Many of the details of this procedure are given in Ref. 24 (and in Refs. 29 and 30 therein). Here we will only give the basic formulas which relate the energy-band structure to experimental quantities of interest to us.

The most significant difference between Ref. 24 and the present work is in the algorithm for calculating photoemission energy distributions (PED's) below the x-ray limit. In the small-$h\nu$ range, we have shown[19,20] that for cleaved $\langle 111\rangle$ single-crystal Ge, the anisotropy of transport and escape must must be incorporated into the photoemission model to produce theoretical spectra which reproduce the major features of the experimentally observed spectra. The modified formulas for low-$h\nu$ PED's will be summarized here, and are described in more detail in the Appendix.

In the following formulas, the band index n will refer to an occupied state $[E_n(\vec{k}) \le E_F]$, while n' will be an unoccupied (conduction) band index.

The optical constants are obtained by first calculating the imaginary part of the dielectric function at photon energy $h\nu$:

$$\epsilon_2(h\nu) = \frac{64\pi^2}{3h^2\nu^2a^3} \sum_{n,n'} \int d^3k \times |\vec{P}_{nn'}(\vec{k})|^2 \, \delta(E_{n'}(k) - E_n(k) - h\nu) , \quad (3.6)$$

where $\vec{k}$ is in units of $2\pi/a$, and the band energies, photon energy, and $|P_{nn'}|^2$ (the optical matrix element squared) are in Ry. In this, and in following formulas, we have averaged over all light polarization directions. $\epsilon_1(h\nu)$ is then obtained by Kramers-Kronig analysis and can be used in conjunction with $\epsilon_2(h\nu)$ to obtain other optical properties.

The one-electron density of states $N(E)$ is obtained from

$$N(E) = \frac{1}{4} \sum_n \int d^3k \, \delta(E - E_n(\vec{k})) \quad (3.7)$$

(in states/Ry atom, both spins), where again E is in Ry and $\vec{k}$ is in units of $2\pi/a$. The factor of $\frac{1}{4}$ (rather than $\frac{1}{2}$ as in Ref. 24) reflects the fact that there are two atoms per unit cell.

The δ functions in (3.6) and (3.7) confine the integrals to surfaces in $\vec{k}$ space, and the resulting surface integrals are done on a uniform cubical mesh of ~1500 points in the $\frac{1}{48}$ of the BZ defined by $k_x \ge k_y \ge k_z \ge 0$. This conversion to surface integrals, as well as the integration method, are described in Refs. 23–25.

For calculating the PED's, two direct-transition models are used. One, called the "isotropic" model, is the usual[22] "three-step model," in which the photoemission process is described as the successive application of formulas describing the probability of (i) optical excitation (ii) propagation of the excited electron to the surface, and (iii) transmission of the excited electron through the surface.

This model was modified by Janak *et al.*[23,24] to describe electron transport [step (ii)] and the production of inelastically scattered electrons more completely. We have used Janak's computer codes for this model, as well as for the calculation of $N(E)$ and $\epsilon_2(h\nu)$.

We have found that certain approximations in this isotropic model are too severe for the case of cleaved, single-crystal Ge, in which the angle-integrated photoemission distribution of electrons from a single (111) face is measured. In the isotropic model, one essentially averages emission through all possible orientations of the sample surface with respect to the BZ (or crystal) axes. In the case of polycrystalline Cu, for example, for which this model has been used,[22,24] the sample may consist of polycrystallites which are oriented with many different crystal faces exposed so that the type of averaging implicit in the isotropic model is approximated in the experiment. (Smith has also extensively studied evaporated transition metals and has used similar formulas.[26])

For single-crystal Ge we have found that an "anisotropic" model for the primary emission, in which steps (ii) and (iii) describe transport to, and escape through, a particular crystal face, gives low-photon-energy PED's which agree much better with experiment than do those predicted by the isotropic model.[19,20] This model is described briefly here and in more detail in the Appendix.

The primary (unscattered) electron distribution originating at energy E_i, excited by photons of energy $h\nu$, and escaping through a crystal face with unit normal vector $\hat{n}$ is given by

$$N_p(E_i, h\nu, \hat{n}) = \alpha(h\nu)[\eta(h\nu)]^{-1} \times \sum_{nn'} \int d^3k \, [|\vec{P}_{nn'}(\vec{k})|^2 \, \delta(E_n(k) - E_i)$$

$$\times \delta(E_{n'}(\vec{k}) - E_i - h\nu)]\, D_{n'}(\vec{k}, \hat{n}) T_{n'}(\vec{k}, \hat{n}), \tag{3.8}$$

where the three main factors in the integrand (the term in square brackets, $D_{n'}$, and $T_{n'}$) correspond to the three steps described above (optical excitation, transport to the surface, and transmission through the surface).

Equation (3.8) gives the distribution of emitted primary photoelectrons per absorbed photon [$\alpha(h\nu)$ is the absorption coefficient] if $\eta(h\nu)$ is defined

$$\eta(h\nu) \equiv \int_{-\infty}^{0} dE_i\, P_0(E_i, h\nu), \tag{3.9}$$

$$P_0(E_i, h\nu) \equiv \sum_{n,n'} \int d^3k\, |\vec{P}_{nn'}(\vec{k})|^2\, \delta(E_n - E_i) \times \delta(E_{n'} - E_i - h\nu). \tag{3.10}$$

Here P_0 is the distribution of optically excited electrons and is used to determine the secondary electron distribution $N_s(E_i, h\nu)$ via the Kane random-$\vec{k}$ model[44] as described in Ref. 24.

The effective escape depth for electrons in final-state $(n', \vec{k})$ is given by

$$D_{n'}(\vec{k}, n) = \frac{\tau(E_{n'}(\vec{k}))\vec{\nabla}_{\vec{k}} E_{n'}(\vec{k}) \cdot \hat{n}}{1 + \alpha\tau\vec{\nabla}_{\vec{k}} E_{n'}(\vec{k}) \cdot \hat{n}} \tag{3.11}$$

when the photon intensity varies as $\alpha e^{\alpha \hat{n}\cdot\vec{r}}$ (α is the optical absorption coefficient and $\hat{n}\cdot\vec{r} < 0$ for $\vec{r}$ within the solid, and $\vec{r} = 0$ at the surface). The final-state electron lifetime τ is determined by the inelastic electron-electron scattering rate obtained from the Kane random-$\vec{k}$ model[44] as described in Ref. 24. For this model, $\tau = \tau(E_{n'})$.

The surface transmission probability $T_{n'}(\vec{k}, \hat{n})$ in Eq. (3.8) is obtained by using the formula for classical transmission through a specular surface with a barrier of height V_0 which is only a function of the coordinate perpendicular to the surface,

$$V_{\text{surf}}(\vec{r}) = V_{\text{surf}}(\hat{n}\cdot\vec{r}) = \begin{cases} 0, & \hat{n}\cdot\vec{r} \ll 0 \\ V_0, & \hat{n}\cdot\vec{r} \gg 0 \end{cases} \tag{3.12}$$

(see Appendix). The final-state wave function is then decomposed into plane waves:

$$\psi_{n'\vec{k}}(\vec{r}) = \sum_{\vec{G}} C^{n'}_{\vec{G},\vec{k}}\, e^{i(\vec{k}+\vec{G})\cdot\vec{r}}\,. \tag{3.13}$$

The individual plane-wave components in (3.13) are tested for their ability to traverse the surface barrier in Eq. (3.12) (which conserves $\vec{k}+\vec{G}$ parallel to the surface). The classical transmission probability of a given plane wave in Eq. (3.13) is (see the Appendix)

$$t^{n'}_{\vec{G},\vec{k}} = \begin{cases} 0 & \text{for } E_{n'}(\vec{k}) - V_0 - \dfrac{\hbar^2(\vec{k}+\vec{G})^2_{11}}{2m} < 0 \\ 1 & \text{for } E_{n'}(\vec{k}) - V_0 - \dfrac{\hbar^2(\vec{k}+\vec{G})^2_{11}}{2m} > 0 \end{cases}. \tag{3.14}$$

Finally we obtain

$$T_{n'}(\vec{k}, \hat{n}) = \sum_{\vec{G}} t^{n'}_{\vec{G},\vec{k}} \left| C^{n'}_{\vec{G},\vec{k}} \right|^2\,, \tag{3.15}$$

where we have summed probabilities (and not amplitudes) in (3.15) since separate beams leaving the sample do not overlap at the detector.

The final result for the total distribution of primary plus secondary electrons

$$N(E_i, h\nu, \hat{n}) = N_p(E_i, h\nu, \hat{n}) + N_s(E_i, h\nu) \tag{3.16}$$

is then normalized to the total yield at one value of $h\nu$ in order to determine the inelastic scattering matrix element.[24] As described in Ref. 24, the $\vec{k}$-space integrals in Eqs. (3.8) and (3.10) are done by a modification of the Gilat-Raubenheimer method.[45]

The resulting direct-transition model for photoemission differs in some details from previous models which have been applied to semiconductors.[46] The most significant difference is our anisotropic treatment of photoexcited electron transport and escape. This causes certain spectral features is $P_0(E_i, h\nu)$ [Eq. (3.10)] to be severely attenuated if they correspond to optical transitions into final Bloch states which cannot match to a significant propagating current outside of the cleaved surface. Properly emphasizing peaks in P_0 according to the experimental conditions will be one of the important factors enabling us to understand in Sec. V the $\vec{k}$-space origin of peaks in the PED's in Fig. 3.

IV. ONE-ELECTRON DENSITY-OF-STATES OVERVIEWS

In this section we present measurements of one-electron density-of-states $N(E)$ features for the core levels, valence bands ($E = E_i \leq 0$; $E = 0 = E_v$, valence-band edge), and filled intrinsic surface states (occupied states); and for the unoccupied intrinsic surface and conduction-band states ($E > 0$). These measurements, besides supplying a graphic overview of features such as the spectral density of core levels and surface states, will also provide several energy-band critical-point values to be used in later sections for producing a model of the valence- and conduction-band structure of Ge.

A. Occupied-state overview

Figure 6 presents the basic data to be used for obtaining a photoemission density of states (PDS)

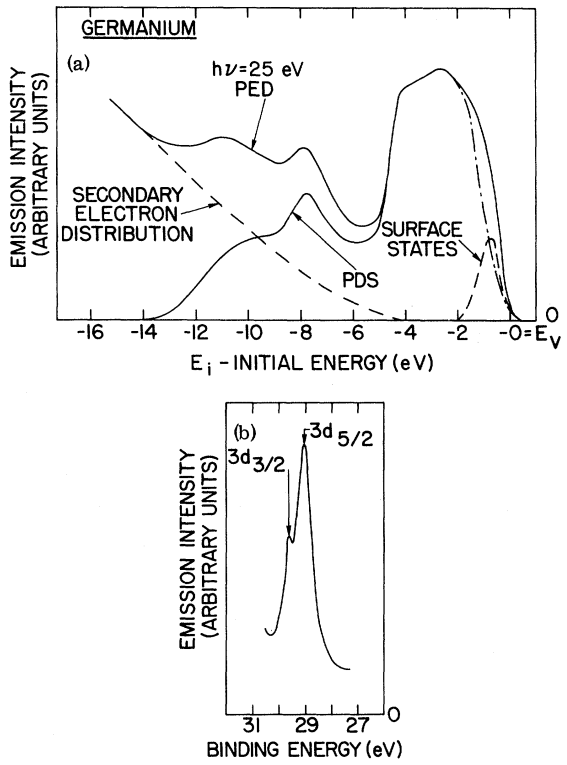

FIG. 6. (a) PED is the experimental $h\nu = 25$ eV spectrum. Subtraction of an estimated secondary electron distribution (dashed) and a surface distribution (dashed; from Ref. 47) results in a photoemission density of states (PDS; see Ref. 13), which represents features in the bulk density of states. (b) Emission spectrum from the spin-orbit-split $3d$ level ($\Delta = 0.55$ eV). Binding energy is referred to zero at E_v.

for occupied electronic levels. In Fig. 6(b) we give the Ge $3d$-core-level emission spectrum ($h\nu = 40$ eV) versus electron binding energy (the negative of the initial energy E_i). In Fig. 6(a) we show an emission spectrum for the valence-band region, obtained at $h\nu = 25$ eV (in the XPS regime) which represents features in $N(E_i)$.

Figure 6(b) shows the Ge $3d$ level as a spin-orbit-split doublet, with the $d_{5/2}$ level lying higher than the $d_{3/2}$ level, a spin-orbit splitting $\Delta_{so} = 0.58 \pm 0.05$ eV, and a linewidth [full width at half-maximum (FWHM)] of $2\Gamma = 0.4 \pm 0.1$ eV (corrected for the 0.25-eV experimental resolution[18]). The $d_{5/2}$ binding energy[18] is 29.1 ± 0.1 eV.

In order to obtain a valence-band photoemission density of states (PDS), we perform two subtractions on the $h\nu = 25$ eV spectrum for -13 eV $< E_i \lesssim E_v = 0$. As described previously[28] we subtract a smooth, structureless background from the total emission spectrum, corresponding to the secondary (inelastically scattered) electron distribution, which is shown in Fig. 6(a). Also, in Fig. 6(a) we subtract a distribution corresponding to the spectral distribution of occupied surface states previously determined for Ge,[47] normalized by assuming that all of the emission for 0.5 eV $\lesssim E_i \lesssim E_v$ is surface-state emission. Failure to perform such a surface-state subtraction in a previous paper (Ref. 28) led to an incorrect assignment of the position of the critical point $L_{3'}$. The separate PDS's for occupied bulk and surface states are then displayed in Fig. 8.

B. Unoccupied-state overview

Features in the unoccupied surface and conduction-band density of states are determined[29] (as described in Sec. II) by measuring the partial yield $Y_p(h\nu, E^*_{\text{fixed}})$ for both a clean, vacuum-cleaved sample, and for a sample which was purposefully contaminated with about a monolayer of Sb (to remove the surface states). Figure 7 gives Y_p for a clean surface (solid line) for $E^* = 4$ eV and for $28 \lesssim h\nu \lesssim 38$ eV, a region in which emission corresponding to the empty surface states and low-lying conduction bands is seen. For an Sb-contaminated surface the low-$h\nu$ edge changes (dashed line), corresponding to the removal of the empty surface states. (The dashed line for Sb-contaminated Ge is not continued to larger values of $h\nu$ as the spectrum contains Sb-associated emission at larger $h\nu$.) The difference between these two curves, which corresponds essentially to the empty-surface-state distribution, is also shown. It appears as a doublet since Y_p contains contributions from transitions for both components of the $3d$ doublet. The emission corresponding to

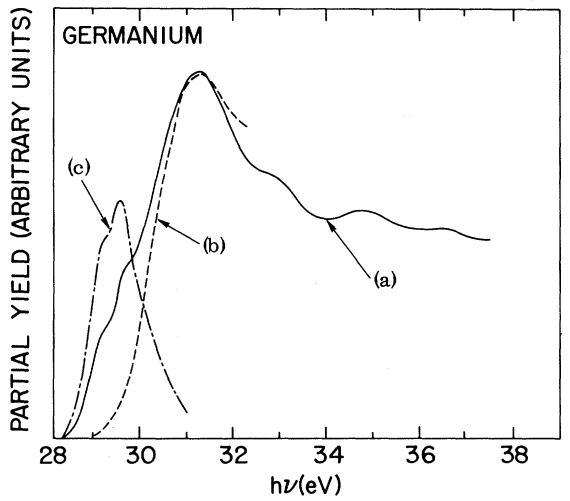

FIG. 7. (a) Partial yield $Y_p(h\nu)$ from a cleaved Ge (111) surface. (b) Y_p for an Sb-coated surface (~ 1 monolayer of Sb), with surface states removed. (c) Difference curve ($\times 2$) representing surface-state partial yield. This difference curve shows both $3d_{5/2}$ and $3d_{3/2}$ transitions (from Ref. 29).

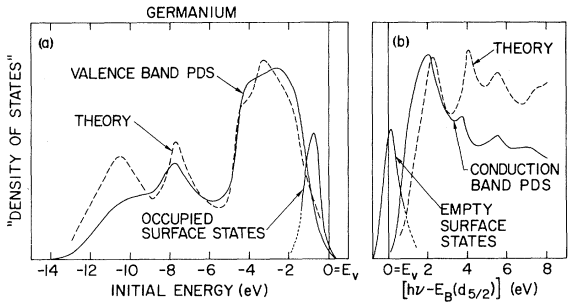

FIG. 8. (a) Experimental valence-band PDS (solid) and surface-state distribution, representing bulk and surface one-electron density-of-states $N(E)$ overviews. Theoretical $N(E)$ from bands obtained from potential I of Table I is dashed. (b) Conduction-band and surface-state PDS (solid) from Ref. 29 are compared with the theoretical conduction-band state density $N(E)$ from potential I of Table I.

the conduction bands alone (dashed line in Fig. 7 for $h\nu < 31-32$ eV, solid line at larger $h\nu$) shows three conduction-band features, which are broadened owing to transitions from both the $d_{3/2}$ and the $d_{5/2}$ level to the conduction band. These contributions result in a broadening in the conduction-band density-of-states features in Fig. 7. To obtain the final photoemission density-of-states overview for Ge for the empty states, the separate $d_{3/2}$ and $d_{5/2}$ contribution to Y_p in Fig. 7 are separated (assuming a 2:3 intensity ratio) and the resulting empty-state density overviews are summarized in Fig. 8.

C. Comparison of state density overviews with theory

We now compare a theoretical $N(E)$ for bulk Ge with the overviews in Fig. 8 in order to obtain certain energy-band positions using the procedure discussed in Ref. 28. The unoccupied-state spectra in Fig. 8 are plotted versus $E = h\nu - E_B(d_{5/2})$, where $E_B(d_{5/2})$ is the $3d_{5/2}$ binding energy measured with respect to E_v, and the experimental spectra have been deconvolved and only the $d_{5/2}$ component plotted. We note that the apparent overlap of the empty-surface-state distribution with the valence-band edge is an artifact which is due to a total instrumental broadening plus core-hole lifetime broadening of ~0.7 eV in the partial-yield measurement.

Figure 8 shows (dashed) a bulk one-electron density of states $N(E)$ (broadened) for the valence and conduction bands determined by the Hamiltonian described by Eqs. (3.1)–(3.5), using pseudopotential I of Table I. This theoretical calculation will be discussed in more detail in Sec. VI. It represents our final "best" fit (in a certain sense) to all the data which will be presented in this paper, and typically represents a fit to better than ~0.3 eV to 16 energy-band positions and optical transitions over a 26-eV range centered on the gap. The energy bands from this calculation are shown in Fig. 9. The broadening of $N(E)$ simulates that in the experiment, as discussed in Ref. 28, and was done using a Lorentzian function of full width at half-maximum $2\Gamma \approx 0.25$ eV at E_v, with the broadening increasing linearly into the valence or conduction bands to a value of $2\Gamma = 0.75$ eV for energies 12 eV away from E_v.

The relation of certain energy-band-calculation critical-point energies to spectral features in $N(E)$ is determined from Fig. 9. Experimental values for these critical points for both valence- and conduction-band states are determined by comparing corresponding experimental and cal-

TABLE I. Parameters for crystal Hamiltonian. Local pseudopotential $[V(G)]$, $l=2$ nonlocal strength A_2 and well radius R_2, and energy-nonlocal coefficient α [see Eqs. (3.1)–(3.5)] used in various calculations reported in this paper. All energies are in Ry, while R_2 is in Å. In all cases we used a lattice constant $a = 5.66$ Å.

		$V(G)$ (local potential)			$l=2$ nonlocal		Energy nonlocal
Calculation	$G^2/(2\pi/a)=$	3	8	11	A_2	R_2	α
I. Energy and $l=2$ nonlocal		−0.2288	0.0289	0.0554	1.89	0.983	0.0258
II. $l=2$ nonlocal fit only to some bands		−0.2300	0.0303	0.0550	0.742	1.173	0
III. Pandey-Philips[a]		−0.223	0.029	0.0500	0.582	1.225	0
Cohen-Bergstresser[b]		−0.23	0.01	0.0600	0	0	0
A. Local		−0.2439	0.0235	0.0453	0	0	0
B. Energy nonlocal		−0.2338	0.0238	0.0442	0	0	0.0848
C. $l=2$ nonlocal		−0.2304	0.0303	0.0569	0.799	1.172	0

[a]Reference 37. [b]Reference 40.

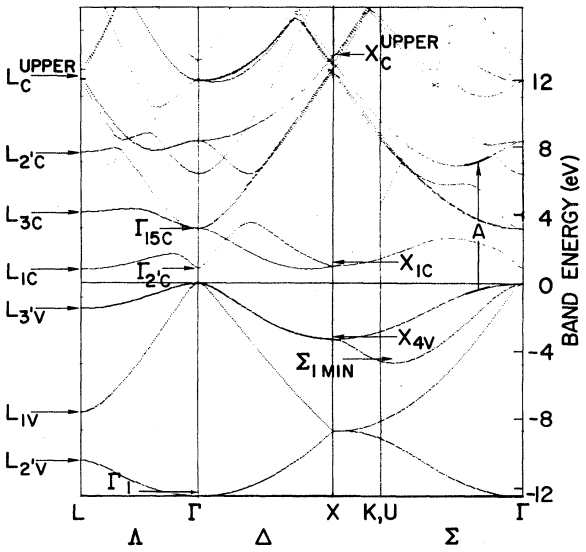

FIG. 9. Theoretical energy bands $E_n(k)$ for valence and conduction bands of Ge from potential I of Table I. Experimental band positions obtained in Secs. IV and V are denoted by arrows. A represents states near those for the optical critical point contributing to peak A in Figs. 13 and 15.

culated spectral features and then referring these calculated features to calculated energy-band locations, as discussed in Ref. 28.

The resulting experimental band positions determined from these $N(E)$ overviews are listed in Table II. These values are the same as those reported in Ref. 28 with three exceptions. The position of L_{1v} is at $E_i = -7.7 \pm 0.2$ eV (present paper, Refs. 19, 20, and 48) and not -7.4 eV as erroneously reported in Table I of Ref. 28 because of a typographical error. The value of $L_{3',v}$ determined here from valence-band overviews (see Table II) is consistent within experimental error with the value determined from direct transition analyses (see Sec. V, Table II of the present paper, and Ref. 20). The value of -1.1 eV reported in Refs. 28 and 48 is incorrect owing to our failure to subtract surface-state emission in obtaining the experimental $N(E)$ overview. Finally, the position of L_{3c} is determined in this section for the first time from conduction-band overviews (see Table II). It was previously also determined from a direct-transition analysis (see Ref. 20, and Sec. V and Table II of the present paper).

We see that the value of L_{3c} (4.1 ± 0.5 eV) determined by this empty-state spectroscopy technique is lower than the more reliable value (4.3 ± 0.2 eV) obtained in Sec. V by a direct-transition analysis. We also note that the conduction-band edge is enhanced in the empty-state overview. These shifts or enhancements can have two origins. First there is the rather straightforward uncertainty in the energy scale and peak positions in Fig. 8(b) introduced by the combination of core-level binding-energy (with respect to E_v) uncertainty and the errors introduced by deconvolution and the finite width of the core hole. Also, however, there may be excitonlike enhancements of edges since the fundamental process giving the experimental data in Fig. 8(b) is a core-to-conduction-state transition. Indeed, the distortion of the conduction-band edge in Fig. 8(b) (comparing experiment with theory) is reminiscent of the conduction-band edge enhancement seen in Si in absorption measurements of the core to conduction-band transition.[49]

We note that the ability to determine certain band positions by *both* the occupied density-of-states overviews in the XPS regime (present section), and by a direct-transition analysis in the "band-structure regime" (Sec. V), provides an internal consistency check on the methods described in this paper.

We now turn, in Sec. V to an analysis of data obtained in the direct-transition-dominated, band-structure regime.

V. DIRECT-TRANSITION ANALYSIS OF ENERGY-BAND STRUCTURE

The aim of this section is to obtain valence- and conduction-band positions from an analysis of photoemission data in the "band-structure regime" ($h\nu \lesssim 15$–20 eV) and from optical data. The motion of dominant emission peaks (whose initial energy E_i is a function of $h\nu$ in the photoemission data) will be reproduced in calculations based on theoretical band structures and an "anisotropic" direct-transition model of the photoemission process (Sec. III, Appendix A) in order to make the correspondence between experimental peaks and particular transitions in the BZ. Several previous studies have utilized various direct-transition analyses.[46] Most notable is the work of Spicer and co-workers (Refs. 31, 50, 51), who used data for $h\nu \lesssim 11.6$ eV (the LiF window cutoff) and attempted to determine which transitions corresponded to various emission peaks by referring to model energy bands plotted along symmetry lines. As Table II shows, certain valence- and conduction-band positions obtained by this method are in reasonable agreement with our assignments (e.g., $L_{3',v}$, X_{4v}) while others (e.g., X_{3c}) disagree. The limitations to this and other previous work[46] were twofold: The small range of $h\nu$ experimentally available did not provide valence-band overviews, which are important in providing a good zeroth-order energy-band calculation for which the valence bandwidths are essentially correct (e.g., see the discussion of CdTe in Ref. 28). Second, a

TABLE II. Energy-band distances from $E_v = \Gamma_{25'v} \equiv 0$ (eV). Figure 9 defines the notation. Spin-orbit splitting (~0.3 eV) has been averaged out. Results are for band positions at 300 K. Error estimates are in parenthesis.

	Valence bands						Conduction bands							
	Γ_{1v}	$L_{2'v}$	L_{1v}	$\Sigma_{1\,min}$	X_{4v}	$L_{3'v}$	L_{1c}	$\Gamma_{2'c}$	X_{1c}	Γ_{15c}	L_{3c}	Γ_{1c}	$L_{2'c}$	L_c^{upper}	X_c^{upper}
Experiment															
Present Work:															
(i) $N(E)$ overviews[a]	12.6 (0.3)	10.6 (0.5)	7.7 (0.2)	4.5 (0.2)	3.15[c] (0.2)	1.4 (0.3)					4.1[d] (0.5)				
(ii) Direct-transition[b] analysis					3.2 (0.2)	1.5 (0.2)	0.8 (0.2)	1.0 (0.1)	1.3 (0.2)	3.25 (0.1)	4.3 (0.2)		7.8 (0.6)	12.6 (1.0)	13.8 (0.6)
Grobman and Eastman[e]	12.6 (0.3)	10.6 (0.5)	7.7 (0.2)	4.5 (0.2)	3.2 (0.2)	1.5 (0.15)	0.84	1.00	1.3 (0.2)	3.25	4.25 (0.2)		7.8 (0.6)	12.8 (0.6)	13.8 (0.6)
Pollack *et al.*[f]	13.0	10.3	7.2												
Spicer and co-workers[g,h,i]				4.5[g] (0.3)	3.1[g] (0.3)	1.7[g] (0.3)				3.14[g] (0.05)	4.1[g] (0.3)				(X_{3c})
					2.9[h] (0.2)	1.4[h] (0.3)					4.0[h] (0.2)	7.2[h] (0.3)	8.2[h] (0.3)		8.3[g] (0.3)
					2.7–3.0[i]	1.6[i]					4.2[i]	6.8–7.0[i]			8.7[i]
Macfarlane *et al.*[j]							0.76								
Theory															
Present paper { potential[k] I	12.85	10.68	7.72	4.73	3.34	1.52	0.85	0.97	1.08	3.34	4.30	6.70	7.97	12.58	13.20
Present paper { potential[k] II	12.62	10.49	7.60	4.62	3.34	1.53	0.84	0.92	1.09	3.23	4.22	6.50	7.76	12.17	12.76
Brust[l] { local	12.0	9.9	6.9	3.8		1.1									
Brust[l] { nonlocal	12.4	10.2	7.6	4.8		1.6									
Pandey and Phillips[m]	12.55	10.42	7.52	4.57	3.23	1.47	0.86	0.99	1.24	3.22	4.35				
Cohen and Bergstresser[n]	11.96	8.87	6.94	3.85	2.57	1.09	0.95	1.17	1.2	3.53	4.28		7.93		

[a] Section IV.
[b] Section V.
[c] $\Sigma_{1\,min} \times 0.7$.
[d] Large error due to uncertainties in empty-state spectroscopy (see Sec. IV).
[e] Reference 20.
[f] R. A. Pollack *et al.*, Phys. Rev. Lett. 29, 1103 (1972); L. Ley *et al.*, Phys. Rev. Lett. 29, 1088 (1972).
[g] Reference 50.
[h] Reference 51.
[i] Reference 31.
[j] Reference 55.
[k] See Table I.
[l] D. Brust, Phys. Rev. B 4, 3497 (1971); and private communication.
[m] Reference 37. The potential in Ref. 42 should give similar results.
[n] Reference 40 and private communication.

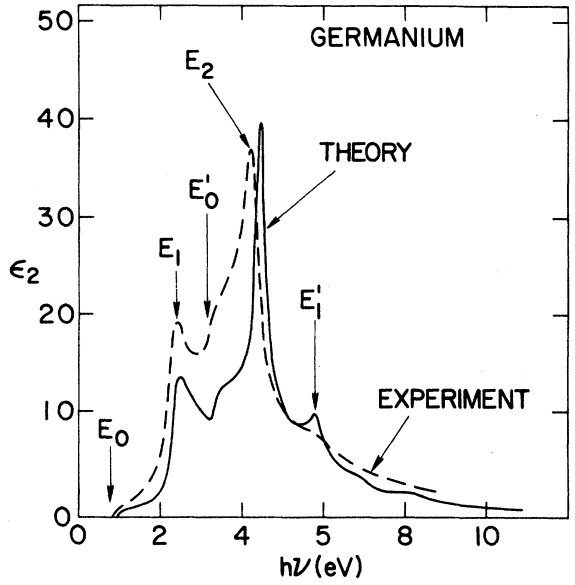

FIG. 10. Experimental imaginary part of the dielectric function, $\epsilon_2(h\nu)$, from Ref. 53 (dashed), and theoretical $\epsilon_2(h\nu)$ (solid), from bands shown in Fig. 9. Pseudo-wave-function matrix elements were used and ϵ_2 (theoretical) was broadened by a Lorentzian of full width $2\Gamma = 0.2$ eV.

photoemission model which is based on an analysis of transitions at general points in the BZ, away from symmetry lines, is a great aid in confirming the identification of certain photoemission features with particular energy-band locations. Previous work along these lines[46] suffered from a lack of data over a wide energy range, incorrect valence bandwidths due to the lack of valence-band overviews,[52] and oversimplified models of the photoemission process.

The energy-band locations determined in this section will be based on an analysis of optical and photoemission spectra from several pseudopotential calculations. The pseudopotentials for these calculations are labeled I, II, and III in Table I.

We will discuss these three potentials in more detail in Sec. VI of this paper, but here given an outline of their similarities and differences. Potential III is the $l=2$ nonlocal pseudopotential of Pandey and Phillips,[37] and formed the basis for our preliminary analysis of Ge energy-band positions in two previous papers.[19,20] Potential I represents a pseudopotential which was adjusted to fit the experimental energy positions obtained in Refs. 19 and 20, and contains both an $l=2$ and energy-nonlocal term [see Eqs. (3.1)–(3.5)]. Potential II was fit to fewer levels and contains no energy-nonlocal term. It is described further in Sec. VI.

The $l=2$ and energy-nonlocal potential represented by pseudopotential I (Table I) will be the principal one used in conjunction with the algorithms described in Sec. III and the Appendix to calculate optical and photoemission spectra in the present paper, and potentials II and III will be used to determine the extent to which results thus calculated are general and not an artifact of one partic-

TABLE III. Optical spectral features and k-space location.

	Experimental[a] position, $h\nu$ (eV)	Theoretical position, $h\nu$ (eV)	Separation of bands at associated symmetry point[i] (eV)	k-space location[i] (units of $2\pi/a$)
E_0	0.99[b]	0.97[g]	0.97 ($\Gamma_{2'c}-\Gamma_{25'v}$)	(0,0,0)
E_1	2.32[c] 2.31[d] 2.34[e]	2.28[g] 2.39[h]	2.37 ($L_{1c}-L_{3'v}$)	Bands 4→5, wide region along Λ, centered on $(\frac{1}{4},\frac{1}{4},\frac{1}{4})$
E_0'	3.20[c] 3.5[d] 3.23[e]	3.25[g] 3.34[h]	3.34 ($\Gamma_{15c}-\Gamma_{25'}$)	Large volume centered on (0.33, 0.24, 0.14)
E_2	4.49[c] 4.5[f] 4.50[e]	4.50[g] 4.40[h]	4.42 ($X_{1c}-X_{4v}$)	Bands 4→5, small region near (0.77, 0.29, 0.16)
E_1'	5.77[c] 5.75[d]	5.78[g] 5.79[h]	5.82 ($L_{3c}-L_{3'v}$)	Near L face, centered on L, bands 3,4→5,6 and 7 (mostly 4→6)

[a]Average of spin-orbit-split components.
[b]Reference 37, Table I.
[c]Reference 54; $h\nu$-modulated $R(h\nu)$.
[d]Reference 53; ϵ_2 peak.
[e]Reference 61; low-field electroreflectance.
[f]Reference 53; $R(h\nu)$ peak.
[g]Reference 42; $dR/dh\nu$.
[h]ϵ_2 feature from Fig. 9 bands.
[i]For Fig. 9 bands, potential I of Table I.

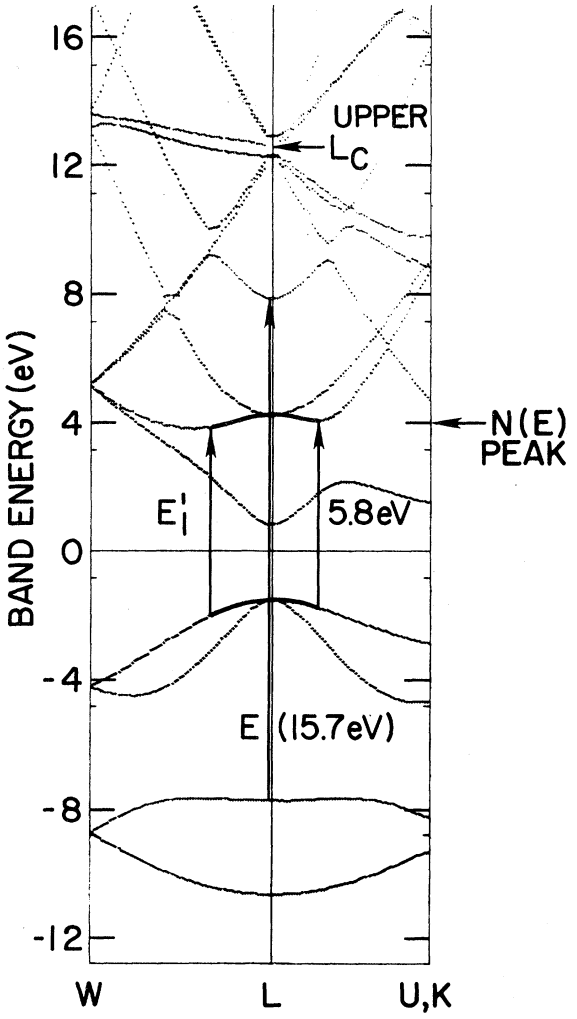

FIG. 11. Ge band structure near L for the same potential as in Fig. 9. Theoretical positions of the peak in $N(E)$ at 4 eV, transitions contributing to the E_1' peak in $\epsilon_2(h\nu)$, and transitions corresponding to the onset of emission from L_{1v} (denoted E; see Figs. 13 and 15) are shown.

ular type of pseudopotential. We note that the one-electron density of states for pseudopotential I has already been displayed in Fig. 8 and used in Sec. IV. The energy bands for this potential are displayed in Fig. 9, which also defines the energy-band notation used in this paper. This calculation will now be used to perform a direct-transition analysis of the experimental energy-band ladders at L, X, and Γ. As our calculations ignore spin-orbit splitting of degenerate bands ($\lesssim 0.3$ eV), energy-band positions will always refer to the center of gravity of spin-orbit-split bands.

A. Energy bands at L

We start with a determination of L_{1c} using $\epsilon(h\nu)$ shown in Fig. 10. The experimental spectrum is taken from Ref. 53, while the theoretical spectrum is from the energy-nonlocal band calculation (potential I in Table I), using the algorithms described in Sec. III. To determine L_{1c}, we consider the E_1 peak in $\epsilon_2(h\nu)$ (Fig. 10), occurring at 2.39 ± 0.03 eV in the theory and experimentally at 2.32 ± 0.02 eV (Table III; three sets of data). Our analysis confirms that this feature is at the energy of the $L_{3'v} - L_{1c}$ separation, but is due to transitions which occur over a large region of $\vec{k}$ space along Λ, centered near $(\frac{1}{4}, \frac{1}{4}, \frac{1}{4})\, 2\pi/a = \vec{k}$. The theoretical value for $L_{1c} - L_{3'v}$ is 2.36 eV, equal to the theoretical E_1 peak position within our computational error. Thus the experimental E_1 position gives $L_{1c} - L_{3'v} \approx 2.3$ eV and, together with $L_{3'v}$ (1.5 ± 0.2 eV) determined below, gives $L_{1c} = 0.8 \pm 0.2$ eV. The absorption measurements in Ref. 55 give directly ~ 0.84 eV for the indirect gap in Ge at $T = 0$ K and ~ 0.76 eV at 300 K (correcting the quoted values for the spin-orbit splitting at $\Gamma_{25'}$), in excellent agreement with our analysis. (Our theoretical position for L_{1c} is 0.85 eV.)

Next we turn our attention to the band positions $L_{3'v}$ and L_{3c} which are related to the optical E_1' peak

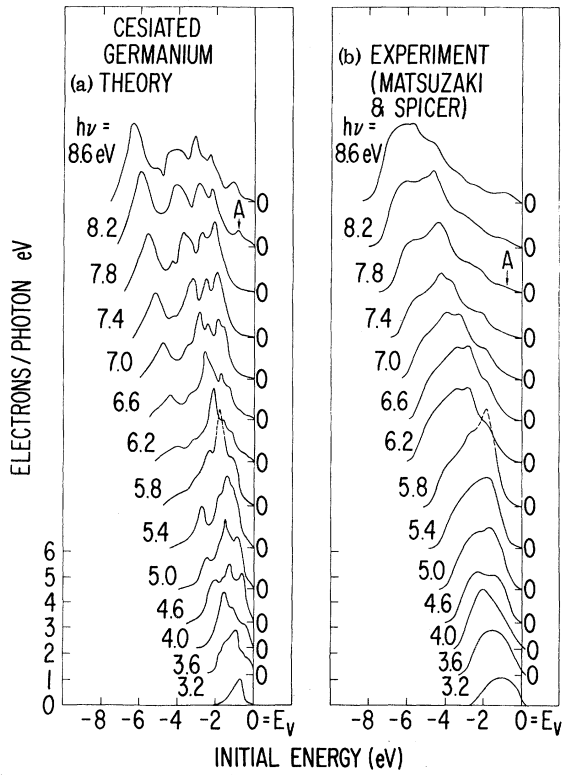

FIG. 12. (a) Theoretical and (b) experimental PED's for cesiated Ge. (a) was obtained using the anisotropic direct-transition model while (b) was taken from Ref. 51. Much of the fine structure in the theoretical and experimental curves agrees to better than 0.5 eV.

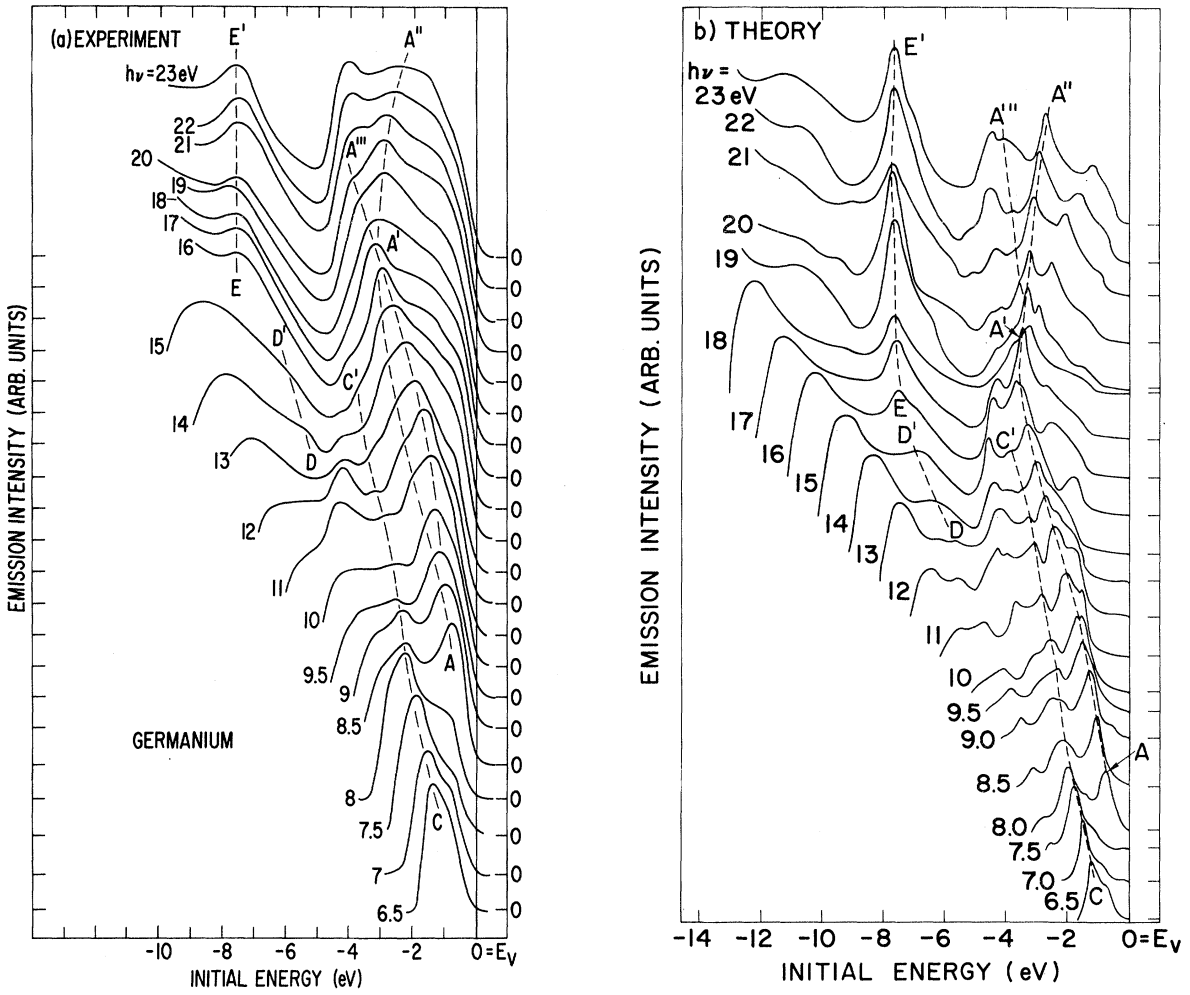

FIG. 13. (a) Experimental PED's with peaks analyzed in Sec. V designated by labeled dashed lines. (b) Theoretical Ge PED's obtained using the (111) anisotropic direct-transition model and energy bands from Fig. 9. (E_i, $h\nu$) positions of labeled transitions are plotted in Fig. 15.

(see Fig. 10). The experimental E_1' feature at $h\nu = 5.8 \pm 0.1$ eV corresponds to a peak in the theory, which also occurs at 5.8 ± 0.05 eV. Zucca and Shen[54] obtain spin-orbit-split modulated reflectivity structures at an average energy of 5.78 eV which arise from the same transitions as those giving the $\epsilon_2(h\nu)$ structure (Table III). Figure 11 shows the bands near L on the L face of the BZ, and the bands contributing to this feature are indicated. From Fig. 9 we see that bands 4 and 6 remain parallel some distance toward Γ along the line Λ. Our direct-transition analysis confirms that the transitions contributing to this optical feature are near L but not confined to the L face. We find theoretically that $L_{3c} - L_{3',v} = 5.8$ eV, so that the E_1' peak position gives the L separation even though much of the contribution to the E_1' peak arises away from L.

With the band-4–band-6 separation at L determined by optical data, we now turn to photoemission spectra for cesiated Ge in order to determine the absolute positions of L_{3c} and $L_{3',v}$ with respect to E_v. Figure 12(b) shows the data of Matsuzaki[51] for cesiated Ge for $3.2 \leq h\nu \leq 8.6$ eV, as well as our theoretical spectra obtained using the anisotropic photoemission model in conjunction with the Fig. 9 (or 11) band structure. In Ref. 50, Spicer identified the strong peak at $E_i = -1.8$ eV for $h\nu = 5.8$ eV as due to transitions at L, and obtained $L_{3',v} = -1.7$ eV (see Table II) and $L_{3c} = 4.1$ eV. We see that our theoretical 5.8-eV spectrum [Fig. 12(a)] reproduces the strong $E_i = -1.8$ eV experimental peak, but $L_{3',v}$ lies 0.3 eV above this value, i.e., at -1.5 eV, with $L_{3c} = 4.3$ eV (Table II). The experimental and theoretical photoemission peak at -1.8 eV $= E_i$ (or at 4.0-eV final energy) thus occurs at a final-state energy 0.3 eV *below* L_{3c} for reasons apparent from Figs. 9 and 11. Namely, the

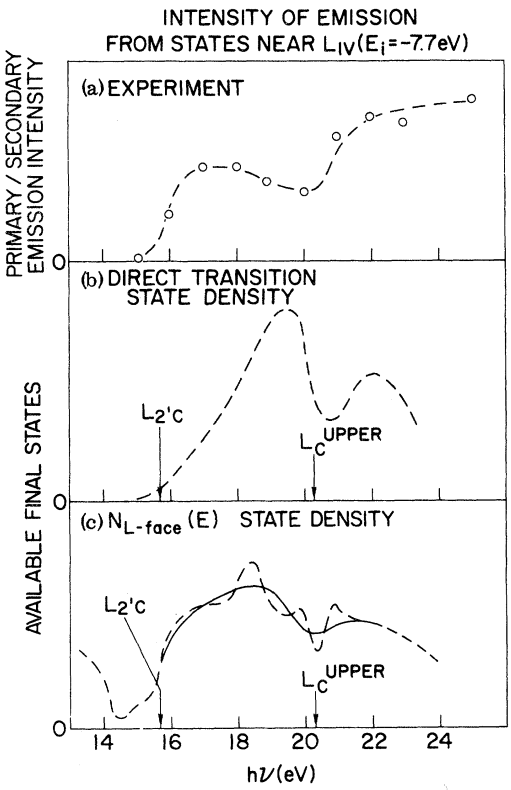

FIG. 14. (a) Ratio of experimental primary/secondary emission intensity from $E_i = 7.7$ eV vs $h\nu$ [from Fig. 13 (a)]. (b) Same ratio (theoretical) as for (a), using Fig. 13(b). (c) Theoretical density of states near the L face (see text) $N_{L\ face}(E)$ vs final-state energy E, plotted vs $E - E_i(L_{1v}) = h\nu$.

strong theoretical $N(E)$ peak at $E = 4.0$ eV (in Fig. 8, theoretical) is seen to come from states away from L on the L face (see Fig. 11), at points surrounding L where the bands have dipped down by 0.3 eV below L_{3c} giving large regions of flat bands which contribute to the large $N(E)$ peak.

Finally, we note that the partial-yield peak in Fig. 8 (experimental) is ~0.25 eV below the theoretical peak, even though the cesiated data agree with the theory as far as this peak location is concerned. As noted in Sec. IV, the partial-yield peaks are subject to errors due to a variety of factors, and may not represent a reliable determination of $N(E)$ features on the scale of a few tenths of an eV. For this reason we consider the value for L_{3c} (4.3 ± 0.2 eV) determined in the present analysis to represent the correct one. Also, note that the Sec. IV value for $L_{3',v'}$ (-1.4 ± 0.3 eV), based on occupied density-of-states overviews, agrees with the present value within experimental error.

We now turn to a determintaion of the high-lying conduction-band levels $L_{2',c}$ and L_c^{upper} (see Fig. 9), the latter being defined as the center of gravity of a set of levels lying ~1 Ry above the gap which are degenerate in the empty-lattice scheme and only slightly split (total splitting ~0.65 eV) by the crystal potential. These levels are determined by considering the intensity of emission from states near L_{1v} as $h\nu$ increases. In Fig. 8 we see a strong peak in the photoemission spectrum at $E_i = -7.6$ eV and also in $N(E)$ (theoretical) at the same position, corresponding to states on and near the L face associated with L_{1v}. Figures 9 and 11 emphasize that while the states associated with this peak are strongly localized on the L face, they are spread over a large region of the face. As $h\nu$ increases, the direct-transition model predicts few final states available for emission from $E_i \approx -7.7$ eV until $h\nu \approx 15.7$ eV, at which point a final-state band dips down at L ($L_{2',c}$; Fig. 11). This prediction is verified both experimentally and theoretically. Figure 13(a) shows experimental PED's for $6.5 \leq h\nu \leq 23$ eV, while 13(b) gives the calculated spectra for the same values of $h\nu$. The line denoted $E - E'$ on this figure shows the emission peak from initial states near $L_{1v'}$ a peak which is weak or absent in the $h\nu \leq 15$ eV spectra but of significant strength at $h\nu = 16$ eV. The onset of the transitions corresponding to this peak is indicated by E in Fig. 11. In Figs. 14(a) and 14(b) we plot the experimental peak intensity at $E_i = -7.7$ eV, normalized to the inelastic electron background, for both the experimental and theoretical spectra of Fig. 13. We also plot, in Fig. 14(c), the density of final states in the region of $\vec{k}$ space near the L face where the band associated with L_{1v} is flat. In all three curves we see an abrupt intensity increase between 15.5 and 16.0 eV, and thereby determine that $L_{2',c}$ (experimental) lies 15.5 ± 0.6 eV above $L_{1v'}$ giving $L_{2',c} = 7.8 \pm 0.6$ eV above E_v. Since the onset is so well defined in the data, it should in the future be possible to refine the position of $L_{2',c}$ by studying the constant initial-state spectrum[56] $N(E_i = -7.7\ \text{eV}, h\nu)$ where E_i is fixed and $h\nu$ varies continuously. This will yield a more refined line shape than we have obtained in Fig. 14(a), where we used only experimental spectra separated by 1-eV steps in $h\nu$.

The determination of L_c^{upper} from Fig. 14 is more uncertain, for several difficulties arise in such a determination. First one must decide whether direct transitions to sharp final-state bands occur, in which case Fig. 14(b) properly represents the experimental variation of emission from $E_i = -7.7$ eV as $h\nu$ varies through the value corresponding to transitions near $L_{1v} \rightarrow L_c^{upper}$. Alternatively, we could argue by referring to Fig. 5 that at these final-state electron energies the momentum broadening of the final-state bands is large in the direction perpendicular to the surface, in which case the density of final states more

correctly describes the variation of the intensity of emission from $E_i = -7.7$ eV vs $h\nu$. In that case the density of final states near the L face [Fig. 14(c)] is the appropriate theoretical quantity to compare with experiment. Reference to Fig. 14 clearly shows that it is this latter quantity [denoted $N_{L\ \mathrm{face}}(E)$] which more nearly corresponds to the experimental intensity for emission from L_{1v} vs $h\nu$. The position of L_c^{upper} is then marked by a dip in $N_{L\ \mathrm{face}}(E)$, corresponding to the opening of the gap at L_c^{upper}. We show a smoothed version of $N_{L\ \mathrm{face}}(E)$ in Fig. 14(c) and compare this curve with the experimental one. While the experimental curve [Fig. 14(a)] is similar to the smoothed version of $N_{L\ \mathrm{face}}(E)$ [Fig. 14(c)], it has a rising background not present in the theoretical curve. (This is probably an artifact of our arbitrary procedure of normalizing to the inelastic background.) Considering this, we identify L_c^{upper} (experimental) with the position of greatest curvature in $N(E_i = -7.7$ eV, $h\nu)$, since this is the feature which is least sensitive to the errors introduced by our normalization procedure. $L_c^{\mathrm{upper}} - L_{1v}$ is thus determined to be 20.3 ± 1.0 eV, giving $L_c^{\mathrm{upper}} = 12.6 \pm 1.0$ eV, which agrees better with the theoretical value obtained using potential I than potential II in Table II. That is, explicitly including a "self-energy" correction improves agreement, although the large experimental error must be considered in assessing the strength of this conclusion. We note that constant initial-state spectroscopy,[56] in which a continuous spectrum versus $h\nu$ is obtained, might help to refine the value of L_c^{upper} and strengthen this conclusion.

B. Energy bands at X

We start with a determination of X_{4v} and X_c^{upper} (Fig. 9) by analyzing a peak which first appears[57] at $E_i \approx -0.7$ eV for $h\nu = 8.2$ eV and then moves further below E_v as $h\nu$ increases. This peak is the most intense feature in low-$h\nu$ spectra. It is labeled $A - A'$ in Fig. 13, and as we shall see is associated with transitions between Γ and the X face of the BZ, and thus contains information about states near X. In Fig. 15 we have plotted the peak positions of Fig. 13 as loci of points placed at the $(E_i, h\nu)$ positions of these peaks. Such a "structure plot" is a plot of what Kane[58] calls "$E_i - h\nu$ images" of photoemission critical points. Such a plot is an excellent way to compare direct-transition features in theoretical and experimental spectra. Also, as Kane[58] has shown, these $E_i - h\nu$ images can be used to identify various types of critical points. We note that an intense low-$h\nu$ peak propagates along the lines $A - A'$ on the structure plot as $h\nu$ increases, reaches a minimum E_i value at $h\nu = 17$ eV for the experimental spectra, and then propagates toward E_v as $h\nu$ increases further $(A' - A'')$. Another set of transitions contribute along a line labeled $A' - A'''$ in Fig. 15, which joins $A - A' - A''$ close to the point $(E_i, h\nu) = (-3.2, 17$ eV), at which position the line $A - A' - A''$ has reached its maximum extent below E_v. Also, Fig. 13(a) shows other direct-transition peaks at $h\nu \geq 17$ eV which appear to converge on the point $E_i = -3.2$ eV, $h\nu = 17$ eV. Kane shows that such a junction of several $E_i - h\nu$ images is a sign that the junction occurs at a value of E_i for which $N(E_i)$ has a critical point [i.e., at which the energy band $E_n(\vec{k})$ is such that $\vec{\nabla}_{\vec{k}} E_n(\vec{k}) = 0$] and, *simultaneously*, at which $\vec{\nabla}_{\vec{k}} E_{n'}(\vec{k}) - \vec{\nabla}_{\vec{k}} E_n(\vec{k}) = 0$. The latter condition, for initial and final bands parallel, defines an optical critical point. As Kane points out, such a conjunction of $N(E_i)$ and optical critical points usually occurs only at points of high symmetry in the BZ. Reference to Fig. 9 then strongly suggests that the $h\nu = 17$ eV transition occurring at $E_i = -3.2$ eV originates at X in the BZ, and a direct-transition analysis confirms this interpretation. In Fig. 15 we show the $E_i - h\nu$ image $A - A' - A''$ for the theory, and note that its behavior is identical to that of the experimental one. Further, by analyzing the contributions to $A - A' - A''$ we determine that as this line approaches its minimum E_i value at $h\nu = 16.5$ eV, the transitions contributing to it approach X. (The theoretical $E_i - h\nu$ position of transitions from X_{4v} to X_c^{upper} is indicated in Fig. 15.) Note that $A - A' - A''$ (theoretical) does not intersect the E_i position corresponding to X_{4v}, but does reach its minimum E_i value at the theoretical value of $h\nu$ corresponding to $X_c^{\mathrm{upper}} - X_{4v}$. Such behavior is probably due to the $\vec{\nabla}_{\vec{k}} E_{n'}(\vec{k})$ factor in Eq. (3.11). In the direct-transition model, in which $\vec{k}$ is rigorously conserved, the final-state group velocity is zero at a critical point and one does not obtain a

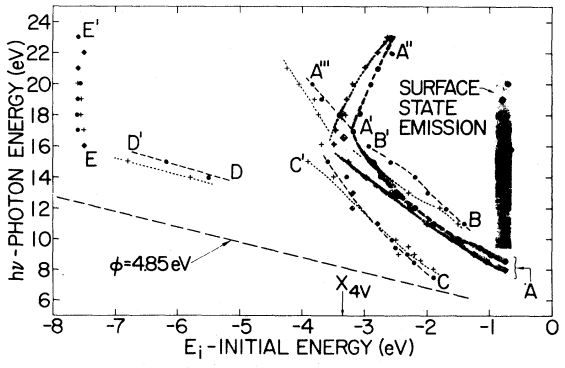

FIG. 15. Position of theoretical (dotted) and experimental (dashed) $(E_i, h\nu)$ images of peaks from Fig. 13. Transitions below the line labeled $\phi = 4.85$ eV are inaccessible for clean, cleaved (11) Ge. Diamond marks the $(E_i, h\nu)$ position of transitions from X_{4v} to X_c^{upper} for the theoretical energy bands.

contribution from the critical point itself. However, spectra computed using energy bands obtained from pseudopotentials II and III in Table I gave a line $A-A'-A''$ which did reach its maximum excursion exactly[19] at the $(E_i, h\nu)$ position corresponding to $(X_{4v}, X_c^{\text{upper}} - X_{4v})$. One reason this can occur in our $\vec{k}$-conserving direct-transition model is that we have made a piecewise-linear approximation to the energy bands, so the group velocity can be nonzero and fairly large near such symmetry points. In the experimental situation, the spectral features contributing near A' in Fig. 16 arise in the region of final-state energy in which the direct-transition features in the spectra weaken as $k_\perp^{(2)}$ increases, so that emission even at X is possible.

This discussion leads us to conclude that $E_i = -3.2 \pm 0.2$ eV is the experimental value of X_{4v}, and that X_c^{upper} lies about 17 eV above X_{4v}, at 13.8 ± 0.6 eV. This X_{4v} value is in excellent agreement with the value of -3.15 ± 0.2 eV obtained in Sec. IV from the experimental $\Sigma_{1\ \text{min}}$

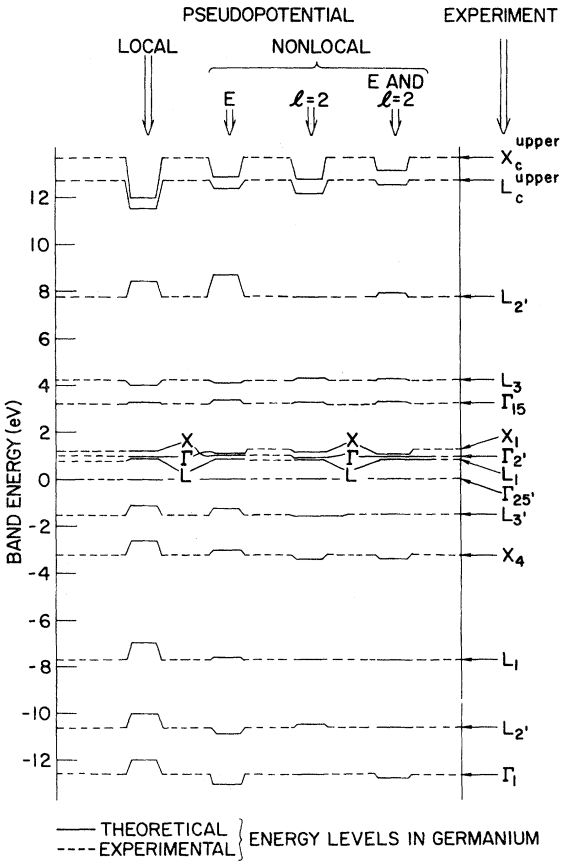

FIG. 16. Experimental band energy positions for Ge (Table II, Fig. 9) are dashed. Theoretical positions are given (solid, horizontal lines) for potentials A, B, C, and I of Table I.

position, using an indirect method. X_c^{upper} is much more uncertain, and appears to lie above the pseudopotential-I theoretical value (Table II) by about 0.6 eV, although the error bound on X_c^{upper} is so large that caution is required regarding this conclusion. For pseudopotential II, with no energy nonlocality, the disagreement is greater.

Finally, we determine X_{1c} from the value for X_{4v} plus the measured value for the E_2 structure in optical data, in conjunction with the theoretical optical spectra. We first note that three recent papers have performed an analysis of the $X_{1c} - X_{4v}$ separation based on optical data. Phillips and Pandey[38] initially reported a value of 4.1 eV $= X_{1c} - X_{4v}$ (at low temperatures below ~80 °K), but corrected this value to 4.5 eV after[37] analyzing electroreflectance data. These authors also report[37] values for X_{4v} and X_{1c} separately which imply that $X_{1c} - X_{4v} = 4.16$ eV. These results are not consistent, and we concur with the $X_{1c} - X_{4v}$ value of 4.5 eV, but not the separate X_{1c} and X_{4v} values. Chelikowsky and Cohen[42] find that they can fit the experimental logarithmic derivative of the reflectivity $R(h\nu)$ quite well using an $l=2$ nonlocal-pseudopotential calculation, and obtain a zero in dR/R near 4.5 eV (which is the experimental position at 0 K) with energy bands for which[59] $X_{1c} - X_{4v} = 4.45$ eV. We verify, using energy bands obtained from potentials I–III in Table I, as well as one[19] with no $l=2$ nonlocality, that in all cases the E_2 peak in $\epsilon_2(h\nu)$ [and in $R(h\nu)$], and $X_{1c} - X_{4v}$ lie within 0.1 eV of each other. Reference 54 gives ~4.45 eV as the position of the zero of $(1/R)$ $(dR/dh\nu)$ at 300 K, and we assign $X_{1c} - X_{4v} \approx 4.5 \pm 0.15$ eV. Using our previous value of -3.2 ± 0.2 eV for X_{4v}, we obtain $X_{1c} = 1.3 \pm 0.2$ eV. Finally, we note that the E_2 peak position of 4.3 eV for $\epsilon_2(h\nu)$ reported in Ref. 53 (see Fig. 10) is possibly wrong by 0.15–0.2 eV. It agrees neither with the reflectivity peak position in the same reference, nor with the Ref. 54 value; our analysis, based on several different band structures, suggests that these values should agree to better than 0.1 eV. Our analysis also suggests that the reason for this discrepancy is that the measured $R(h\nu)$ in Ref. 53 is systematically too low at $h\nu$ greater than 6 or 7 eV, leading to a shift of the $\epsilon_2(h\nu)$ peak at E_2 obtained from a Kramers-Kronig analysis.[60] Table III gives experimental and theoretical values for the E_2 structure for several experiments and pseudopotentials, and shows that the transitions contributing to the E_2 peak occur near $(\frac{3}{4}, \frac{1}{4}, \frac{1}{4})$, in agreement with the analysis of Chelikowsky and Cohen.[42]

C. Energy bands at Γ

We obtain $\Gamma_{2',c}$ from the experimental value for the E_0 critical point (Table III) as 1.0 ± 0.1 eV,

using the Ref. 61 experimental value and verifying from our direct-transition analysis the rather obvious fact that this critical point is completely due to transitions near Γ. The 0.1-eV error bound reflects the fact that our non-spin-orbit-split bands cannot represent the true situation in Ge, with an ~0.3-eV splitting, by better than one or two tenths of an electron volt. (The splitting is not in $\Gamma_{2'c}$, but in $\Gamma_{25'v} = E_v$, the valence-band edge, which is the reference energy.)

Finally, Γ_{15c} is determined from the Ref. 61 E_0' average value of 3.23 eV and our analysis, which shows that the E_0' critical point, which occurs due to transitions over a large region of $\vec{k}$ space away from Γ, nevertheless corresponds to the energy separation $\Gamma_{25'v} - \Gamma_{15c}$ to better than 0.05 eV (see Table III).

VI. DISCUSSION

We will describe here the physical implications of the work presented in Secs. I–V, which did not discuss the physics of the electronic structure in a broad way but rather presented the framework for, and the details of the determination of, the valence- and conduction-band structure of Ge.

A. Crystal potential

A study of the nature of nonlocality in the pseudopotential was performed by attempting to find a "best" fit to the energy-band positions we have determined in the preceding sections (Table II). We studied the ability of local, energy-nonlocal, and angular-momentum-nonlocal ($l=2$) terms in Eqs. (3.1)–(3.5) to fit the Table II experimental positions. This study employed a function of the form

$$\sum_i W_i [E_i(\text{expt}) - E_i(\text{theor})]^2, \tag{6.1}$$

which was minimized with respect to variation of different pseudopotential models. In (6.1) the E_i are the symmetry-point energies listed in Table II (excluding $\Sigma_{1\,\text{min}}$), as well as certain optical transition energies, while the weights W_i were chosen to approximate the inverse square of the experimental uncertainty in the different levels. The function in Eq. (6.1) consists of a total of 16 terms.

Figure 16 graphically presents the result of our study. We first set α and A_2 in Eqs. (3.1)–(3.5) equal to zero, yielding a purely local pseudopotential, and then varied the $V(G)$ (three parameters) for the best over-all fit. Figure 16 demonstrates that the resulting best local pseudopotential (potential A in Table I) yields valence *and* conduction bandwidths which are systematically too narrow, and places $L_{2'c}$ much too high. We have previously[28,48] noted this effect for the valence bands when comparing photoemission density-of-states overviews for a wide variety of semiconductors with theoretical $N(E)$'s for bands fit to optical spectra using only a local pseudopotential. Figure 16 illustrates that this narrowing of the valence bands using only a local potential is a feature common to the upper conduction bands also.

Several authors have attempted to correct this effect with an "effective-mass" approximation, equivalent to our "energy-nonlocal" pseudopotential [α nonzero, but $A_2=0$ in Eq. (3.5)]. Herman[2] used such an approximation to fit a pseudopotential interpolation scheme to a first-principles orthogonalized-plane-wave (OPW) calculation, while in Ref. 43 and in a previous work of ours[19] such calculations were performed in order to fit both optical data and photoemission valence-band $N(E)$ overviews simultaneously.

We varied $V(G)$ and α (four parameters), while keeping $A_2=0$ to get the best energy-nonlocal pseudopotential (potential B in Table I), which resulted in the energy-band positions shown in Fig. 16. There are two major defects in the resulting energy levels: (i) In broadening the conduction bands for a better fit than achieved by the local potential, the valence bands are broadened too far; (ii) $L_{2'c}$ is still fit very poorly, lying ~1.5 eV too high. In addition, X_{1c} and $\Gamma_{2'c}$ are ordered improperly. These observations are in agreement with the arguments of Pandey and Phillips[37] that the energy-nonlocal term alone cannot produce a correct energy spectrum.

That one can do better is obvious from the third column in Fig. 16, where we show the results for the best $l=2$ nonlocal pseudopotential (potential C in Table I). In obtaining this fit we set the energy-nonlocal term equal to zero ($\alpha=0$) and varied $V(G)$ and the $l=2$ radius and strength R_2 and A_2 (five parameters total). Except for L_c^{upper} and X_c^{upper} the fit is excellent—better than a few percent over the entire range of ~20 eV from ~−12 to ~+8 eV.

Comparing the local and $l=2$ potentials, and temporarily ignoring L_c^{upper} and X_c^{upper}, it is obvious that the $l=2$ potential properly corrects the valence bandwidth *and* the position of $L_{2'c}$ while maintaining the correct energy-band positions near the gap, the latter providing a good fit to optical properties. These results thus strongly support the view that $l=2$ nonlocality is the form of nonlocality which best models the physics of the actual crystal potential in Ge. This view was recently discussed in Ref. 37 and was shown to give energy-band separations near the gap whose topology (i.e., critical-point structure) was in accord with electroreflectance measurements. We verify that the topology of the upper conduction bands, namely, the position of bands near $L_{2'c}$ with respect to other bands in the vicinity, is

properly fit only by an $l=2$ component to the pseudopotential, which can change the position of $L_{2'c}$ relative to other states. Reference 19 also demonstrated this fact.

Further support for these views comes from a recent calculation of Chelikowsky and Cohen,[62] who show that an $l=2$ nonlocal pseudopotential produces a much more reasonable bond charge distribution than does a local one, while also correctly predicting the temperature dependence of certain x-ray reflection intensities for both Si and Ge. We note that the present best-fit $l=2$ pseudopotential (potential C in Table I) is quite similar to that in Ref. 37 in the magnitude of the $l=2$ term (A_2) as well as the radius of the interaction (R_2).

Finally, we allowed $\alpha \neq 0$ in addition to varying $V(G)$, A_2, and R_2 (six parameters total) to obtain an "energy and $l=2$ nonlocal" potential (potential I in Table I) which produced the energy levels in column four in Fig. 16. The energy-nonlocal parameter improved the fit slightly, but not in a qualitatively significant manner. As expected, the fits to L_c^{upper} and X_c^{upper} became somewhat better. The $l=2$ nonlocal strength, given by $A_2R_2^3$ (see Table I) is about 60% larger than for fits obtained using purely $l=2$ nonlocal potentials, with A_2 larger and R_2 about 20% smaller. Further, the photoemission spectra calculated with this model are not in as good agreement with experiment as are those calculated using potential III of Table I (compare Fig. 13 of the present paper with Fig. 2 of Ref. 20), although the position of direct-transition features is in excellent agreement with experiment as shown, e.g., by Figs. 9, 10, 15, and 17 of the present paper. While potential I in Table I, containing both $l=2$ and energy nonlocality ($\sim 2\frac{1}{2}\%$), was used to perform the analyses in this paper, it appears that a better way to incorporate self-energy effects might first be to perform a fit to all states except L_c^{upper} and X_c^{upper}, and then to study self-energy effects as a correction to the eigensolutions of this problem. We discuss self-energy corrections below, and suggest as starting potentials for future calculations pure $l=2$ nonlocal potentials II and III in Table I, representing fits by ourselves and Pandey and Phillips,[37] respectively to photoemission and optical data. Our potential II was obtained by fitting to all energy positions in Fig. 17 excluding L_c^{upper} and X_c^{upper}, as well as to the E_1 and E_2 optical gaps.

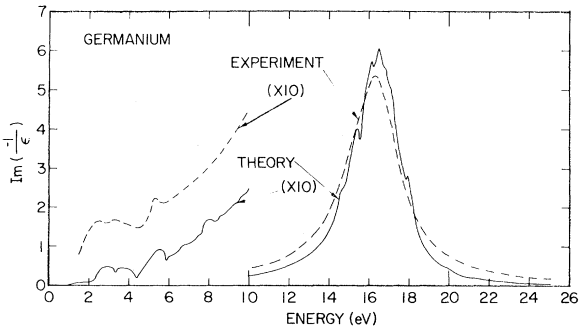

FIG. 17. Theoretical energy-loss function $\mathrm{Im}(-1/\epsilon)$ (solid), obtained using the theoretical $\epsilon_2(h\nu)$ shown in Fig. 10 and a Kramers-Kronig analysis, is compared with the experimental electron energy-loss function (dashed) obtained in Ref. 66.

B. Energy nonlocality in germanium

There are at least two sources of energy nonlocality in simple semiconductors. One is the energy and angular momentum nonlocality introduced during the transformation from a crystal potential to a pseudopotential,[63] and the other is that due to the energy dependence of the exchange and correlation correction to the particle energy. We first consider the extent to which the data suggest significant self-energy corrections, and briefly discuss the incorporation of these effects into calculations.

One piece of evidence for the presence of self-energy corrections is the inability of an $l=2$ nonlocal potential to fit X_c^{upper} and L_c^{upper}. The theoretical value for X_c^{upper} in the fourth column in Fig. 16 is 0.9 eV too low while in Refs. 19 and 20 we showed that an $l=2$ potential (with $\alpha=0$) placed L_c^{upper} and X_c^{upper} too low theoretically. However there is additional evidence which does not depend on these high-lying levels, whose experimental position is rather poorly determined. This additional evidence is obtained by using theoretical photoemission spectra from the energy and $l=2$ nonlocal calculation (potential I of Table I) which were compared to the experimental ones. Feature D-D' (Figs. 13 and 15) is a direct-transition peak which is quite distinct and easily identified in both the theory and the experiment. Its $h\nu$-E_i trace in Fig. 15 occurs ~0.6 eV later in photon energy for the experiment. Similarly, the dominant experimental and theoretical low-energy peak A-A' in Fig. 14 is seen in Fig. 16 to lie at larger $h\nu$ experimentally than theoretically by ~0.5–1.0 eV as $h\nu$ increases from ~8 to ~15 eV. Since the initial bands for these transitions are bands 3 and 4 in the vicinity of the symmetry line Δ, and since $X_{4v}(\text{theory}) - X_{4v}(\text{expt}) \approx 0.15$ eV, this difference is not an initial-state effect at the large photon energies, but is rather a final-state effect—the final-state bands lying ~2–10% higher experimentally than the theoretical ones (in a calculation which already incorporates an $\sim 2\frac{1}{2}\%$ energy-nonlocal correction). For potential III of Table I, which is a purely $l=2$ nonlocal one, a structure plot similar to Fig. 15 shows these effects even more dramatically (Fig. 4 of Ref. 19). Similarly C-C' in Fig.

15, which is due to transitions near Σ and Δ, occurs later in $h\nu$ experimentally as $h\nu$ increases. The feature B-B' also behaves similarly. Thus the $h\nu$-E_i images of transitions which disperse (change their E_i with $h\nu$) rapidly indicate that transitions from a given initial energy occur at larger $h\nu$ experimentally as $h\nu$ increases. This behavior is seen even more strongly in spectra obtained from potentials II and III of Table I (see Fig. 4 of Ref. 19), which do not contain the $2\frac{1}{2}\%$ energy-nonlocal correction of potential I.

A final piece of evidence for a larger experimental initial–final-state separation than is found theoretically is given by the optical transition labeled A in Figs. 9 and 15, which is seen in Fig. 13 as a strong peak which appears at $E_i \approx -0.75$ eV at $h\nu = 8.5$ eV. From Ref. 31 we find that the experimental photon energy for the onset of this transition is ~ 8.2 eV (Fig. II-5 of Ref. 31), while theoretically the threshold is ~ 7.85 eV, i.e., ~ 4% too low, even with the $2\frac{1}{2}\%$ energy-nonlocal term in pseudopotential I.

In summary, for a wide variety of transitions we see that final states are typically $\gtrsim 5\%$ higher experimentally than given by potential I of Table I, and for potentials II and III the difference is even greater. Since these differences are occurring due to transitions between bands at general points in the BZ and not simply at BZ boundary gaps, modifications of the pseudopotential alone are probably not adequate to resolve the discrepancy. The conclusion is then that there is probably a genuine 5–10% self-energy correction for the position of high-lying conduction-band states. That such an effect exists is not surprising when a body of optical and photoemission data spanning an energy range of ~ 2 Ry is being described. Previously, in a direct-transition analysis of Cu data obtained over a wide energy range, an energy-dependent correction to the energy-band positions of ~ 7% was needed to fit excited-state properties.[24]

Finally, we reemphasize the fact that a self-energy term linear in E does not appear adequate to fit the upper levels in Ge. This occurs because the self-energy correction depends not only on the energy of an excitation, but also on the charge density in the vicinity of the excitation.[39] Hole states in the valence bands have wave functions localized near the covalent bonding charge in covalent semiconductors, while electrons in conduction states are rather delocalized throughout the Wigner-Seitz cell.[64] It is possibly this effect which would require a proper description of self-energy effects in semiconductors to proceed by first ignoring self-energy effects and producing a relatively good set of energy bands and wave functions (such as the $l=2$ nonlocal potentials II or III represent). Exchange and correlation corrections could then be calculated in a reasonable way based on the original wave functions and used to correct the energies.[65] An *ad hoc* linear approximation, such as we have attempted, has left most high-energy thresholds too low, for α could not be made very large without destroying the good fit already obtained with an $l=2$ nonlocal potential alone.

Finally, we emphasize that more precise determinations of the positions of high-lying conduction-band features such as L_c^{upper} and X_c^{upper} should be made, perhaps for a variety of semiconductors, before the magnitude of self-energy effects such as we have described can be accurately established.

Other attempts to add nonlocality to the pseudopotential using different models than the ones we present here also improved the agreement with experiment. Brust's model (see Table II) gave good agreement with the energy levels for which he gave results, while Kane's models[65] have improved agreement in the case of Si.

C. Optical properties

In addition to $\epsilon_2(h\nu)$, which was displayed in Sec. V, we have calculated the energy-loss function $[\mathrm{Im}(-1/\epsilon)]$ for Ge. We now discuss the agreement of these optical properties with experiment in a more detailed way. This comparison of theory with experiment will have implications for the f-sum rule and the nature of local-field effects. Figure 10 presents $\epsilon_2(h\nu)$ calculated using energy bands and pseudo-wave-function matrix elements obtained using potential I of Table I. By performing a Kramers-Kronig transformation on ϵ_2, we have obtained the real part of the dielectric function $\epsilon_1(h\nu)$, and then the energy-loss function $\mathrm{Im}(-1/\epsilon)$, where $\epsilon = \epsilon_1 + i\epsilon_2$. In Fig. 17 we show the resulting $\mathrm{Im}(-1/\epsilon)$ and compare it with the same quantity measured by Zeppenfeld and Raether[66] using high-energy inelastic electron scattering. The agreement with experiment is good for the optical interband structure for $h\nu \lesssim 10$ eV, except for the theoretical peak near 8 eV and the over-all magnitude in this region, which is approximately a factor of 2 too low in the theory. The optical structure near 8 eV is associated with a critical point which causes the appearance of the strong peak in photoemission at $E_i \approx -7.5$ eV at $h\nu = 8.2$ eV. This peak (Feature A in Figs. 9, 14, and 16) is seen in the experimental photoemission data of Ref. 31 also and provides experimental evidence that the optical structure near $h\nu = 8$ eV predicted by our model should in fact be present in experimental optical spectra. The fact that it does not appear either in the optical spectra of Phillip and Ehrenreich[53] (Fig. 10) nor in the energy-loss data[66] plotted in Fig. 18 is probably an indication either of experimental resolution, sensitivity, or sample preparation problems or of a large lifetime broadening for the

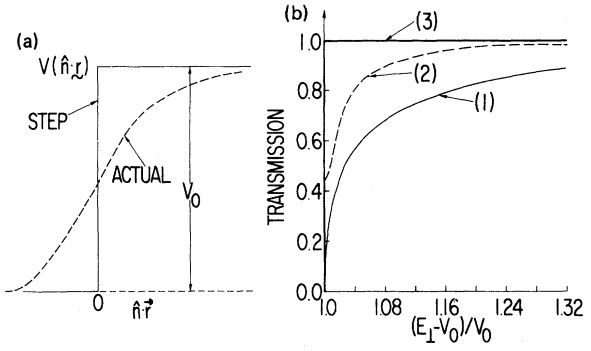

FIG. 18. (a) Ideal surface barrier (solid) and schematic actual one (dashed). (b) Transmission function for (1) the step barrier of (a), using quantum-mechanical formulas; (2) the actual barrier of (a) schematically illustrated for the quantum-mechanical case; (3) the classical transmission function for both barriers of (a).

optical transition.[67]

Turning to the plasmon loss peak in Fig. 17, we note first that the experiment and theory agree very well in both the position and lifetime (energy width) of the plasma. That a one-electron model works so well for the plasmon is not surprising, for the fact that at $q=0$ the transverse (optical) and longitudinal (electron-energy loss) dielectric function are the same[68,69] implies a strong connection between optical and energy-loss measurements.[70]

The agreement between the magnitude of $\mathrm{Im}(-1/\epsilon)$ in the theory and experiment, and the disagreement in the case of $\epsilon_2(h\nu)$ is of some significance for the f-sum rule and the effective number of electrons contributing to $\epsilon(h\nu)$ for $h\nu \lesssim 30$ eV (the onset of $3d$-core-to-conduction-band transitions), as well as the nature of local field effects in Ge. In order to understand this significance, we first briefly review the f-sum rule and the degree to which our theory satisfies it. The pseudopotential model is a strictly one-electron representation of a system with 4 valence electrons/atom and should rigorously yield $n_{eff}(h\nu \to \infty) \to 4$, where

$$n^t_{eff}(h\nu) \equiv \frac{2m}{Ne^2}\int_{\nu_0}^{\nu} \epsilon_2(h\nu)\, d\nu \qquad (6.2)$$

or

$$n^l_{eff}(h\nu) = \frac{2m}{Ne^2}\int_{\nu_0}^{\nu} \mathrm{Im}\left(\frac{-1}{\epsilon}\right) d\nu\,. \qquad (6.3)$$

Here n^l_{eff} and n^t_{eff} represent the effective number of electrons contributing to the transverse or longitudinal dielectric properties up to frequency $h\nu$.[53] In Eqs. (6.2) and (6.3), m is the electron mass and N is the atom density in the solid. Our result for $n^t_{eff}(h\nu \to \infty)$ is 3.64 (91% of 4), while for $n^l_{eff}(h\nu \to \infty)$ we obtain 3.58 electrons/atom. These values are a test of various approximations made in obtaining ϵ_2 from the pseudopotential. Especially tested are (i) the extent to which truncation of the wave functions due to solution of Eq. (3.5) using the Löwdin scheme[40] decreases the pseudo-wave-function matrix element from the exact one-electron solution to Eq. (3.5) and (ii) the degree to which the Gilat-Raubenheimer integration scheme[24,45] used for performing the integral in Eq. (3.6) represents the actual value of the integral; and (iii) the Kramers-Kronig analysis used to obtain ϵ_1 from ϵ_2 is tested by the agreement between n^t and n^l. [The energy bands are known over a wide enough energy range (see Fig. 9) that truncation of the $h\nu$ integrals in Eqs. (6.2) and (6.3) probably is not significant in reducing n_{eff} below 4 by the amount indicated here.] Our values for n^l and n^t agree to about 2%, which verifies that the Kramers-Kronig analysis was properly performed. The reduction of n_{eff} by ~ 10% below 4 electrons/atom for our model probably represents the truncation of the wave function in the Löwdin scheme used for diagonalizing Eq. (3.5). A loss of ~ $2\frac{1}{2}$% of the part of the wave function contributing to $\langle \psi_{n\vec{k}} | \vec{P} | \psi_{n'\vec{k}} \rangle$ causes the matrix element to be reduced by ~ 5% and the sum rule by ~ 10%. For this reason the 10% reduction of n_{eff} for our model is surprising good, since the Lowdin scheme was truncated when the Hamiltonian matrix was large enough to give eigenvalue convergence, but the wave functions have probably not yet converged, owing to the variational theorem.

Returning to Fig. 17, we see that the area under the experimental curve is very nearly equal to that under the theoretical curve, which would give an experimental n^l_{eff} which is between 3.5 and 4 electrons/atom. Such an n^l_{eff} is also consistent with the measured plasma frequency $\hbar\omega_p(\mathrm{expt}) = 16.2 \pm 0.1$ eV. The reason for this is that the valence-electron contribution to $\epsilon_2(h\nu)$ is concentrated near the Penn gap value[71] of $h\nu = 4.3$ eV $= \hbar\omega_g$ (see Fig. 10), which yields a plasmon at[72]

$$\omega_p^2 = (\omega_p^0)^2 + \omega_g^2\,, \qquad (6.4)$$

where ω_p^0 is the plasma frequency of free electrons. For the Ge atom density and 4 electrons/atom one obtains $\hbar\omega_p^0 = 15.59$ eV, which results in $\hbar\omega_p = 16.17$ eV, in excellent agreement with experiment. The model[72] leading to Eq. (6.4) then also predicts $\epsilon_1(0) = 14.14$. A more realistic model, which takes $\epsilon_2(h\nu)$ to have the spectral shape predicted by us, but with its amplitude enhanced to give an n_{eff} of 4, results in $\epsilon_1(0) = 12.96$. The experimental value for $\epsilon_1(0)$ is 16.0, which includes the contribution just calculated plus the $3d$-core polarizability contribution (which is probably[72] less than 1). We thus see that an n_{eff} of 4 electrons/atom for Ge leads to the correct ω_p and close to the observed plasma peak intensity shown in Fig. 17, but then does not

provide a large enough $\epsilon_1(0)$. Phillip and Ehrenreich obtained $n_{eff}(h\nu)$ for several semiconductors from optical constants based on normal-incidence reflectance data and obtained an $n_{eff}(h\nu)$ which does not reach an asymptotic value as $h\nu$ increases but rather rises through 4 electrons/atom at 9.5 eV, 5 electrons/atom at 18 eV, and continues to rise for larger $h\nu$. Indeed, the Phillip-Ehrenreich curve for $\epsilon_2(h\nu)$ is greater than ours over much of the photon energy range, especially between 2 and 4 eV (see Fig. 10), giving rise to a larger n_{eff} than we obtain.

The true value for n_{eff} for Ge (due solely to valence excitations) is probably greater than 4, in order to produce the proper value of $\epsilon_1(0)$, but may not be as large as that measured by Phillip and Ehrenreich.

The contradictory results for n_{eff} are discussed in a paper by Feuerbacher *et al.*,[73] who conclude that better optical data are needed to resolve the issue. The significance of the question is that the amount by which n_{eff} exceeds 4 electrons/atom will experimentally determine the size of the correction to pseudo-wave-function matrix elements caused by orthogonalizing them to the $3d$-core states.[53,74] Such orthogonalization increases the theoretical $\epsilon_2(h\nu)$ [and $\mathrm{Im}(-1/\epsilon)$] above the values shown in Fig. 10 (and in Fig. 17) and would improve agreement with experiment. It is important to know if it is simply this correction to the pseudo-wave-functions which is needed in Fig. 10, or whether a more significant physical effect is occurring, such as local-field corrections. The nature of such corrections is at present poorly understood,[75] and knowing whether such effects occur in Ge would contribute important information to the solution of this fundamental problem (also, see Ref. 60).

We note at this point that the experimental E_2 peak in $\epsilon_2(h\nu)$ in Fig. 10 occurs at ~4.3 eV, 0.2 eV lower than we have placed it. However, as discussed in Sec. V, the ϵ_2 experimental peak is derived from a Kramers-Kronig analysis of reflectivity data, which is a procedure which subjects ϵ_2 to errors arising from some uncertainties in the absolute value of $R(h\nu)$, the reflectivity. We have obtained a theoretical $R(h\nu)$ corresponding to the theoretical $\epsilon_2(h\nu)$ from Fig. 10 and find that its E_2 peak agrees with that of Phillips and Ehrenreich[53] to better than 0.1 eV. Our $R(h\nu)$ above 10 eV is greater than that in Ref. 53 by more than a factor of 2 over a wide energy range,[60] and leads us to believe that the experimental E_2 peak position in ϵ_2 may be ~0.2 eV in error. This view is substantiated by the fact that at least three separate authors,[37,42,59,61] interpreting more direct electroreflectance and wavelength-modulated $R(h\nu)$ data, have concluded that the E_2 transition occurs at 4.4–4.5 eV.

Finall, we remark that for a wide variety of nonlocal as well as local potentials which we have used, ϵ_2 peak positions tend to coincide to better than typically 0.2 eV with symmetry-point band separations (Table III) even though the actual transitions giving the large contribution tend to be over regions of $\vec{k}$ space removed from symmetry points. Previous authors[1–4] have noted this effect for local-pseudopotential calculations, but we have shown that this is a more general effect, even though nonlocality can change some features of band-structure topology.

We conclude that the theoretical model not only provides a good description of photoemission overview and direct-transition data (see Figs. 8, 13, and 15 and the Appendix), but also provides an excellent description of optical and energy-loss data for Ge (see Figs. 10 and 17 and Ref. 42) over a wide energy range. We have also seen that better experimental data, as well as a better understanding of core-orthogonalization and/or local field effects would be useful for a deeper understanding of optical properties.

D. Conclusions

The present paper has shown that one-electron theory and the idea of direct, $\vec{k}$-conserving optical transitions are useful for describing many features in photoemission and optical data over a wide electron band energy range (~26 eV), centered about the gap. In addition, the success of an anisotropic model of transport and escape in improving the agreement of theoretical photoemission spectra with experiment is another[76] demonstration that for cleaved semiconductors some momentum information survives the photoemission process.[76]

We have presented a detailed study of the position of the energy levels at L, Γ, and X and have used the experimental values to study the nature of the pseudopotential in Ge, confirming the need for a large $l=2$ angular momentum nonlocal component in order to properly describe energy bands over a wide range.

We have identified several areas where further calculations and data will lead to new results. The existence of self-energy corrections to excitation energies, varying nonlinearly with energy, are suggested by this work to be of the order of 5–10% of the one-electron energy for the high-lying conduction bands. However, this possibility needs to be confirmed by new data, which could be of several types. Constant initial-state spectroscopy,[56] in which the photoemission intensity from a fixed initial energy E_i is measured as $h\nu$ increases, could be used to determine X_c^{upper} and L_c^{upper} with more precision, increasing the extent of which self-energy effects are understood. Similarly, more pre-

cise high-lying conduction-band information could be obtained using electroreflectance to study core-level–to–conduction-band transitions, as Aspnes and Olson have recently demonstrated.[8,77]

Improved optical data obtained over a wide range of photon energies using synchrotron radiation and ultra-high-vacuum-cleaved samples should improve the precision with which we know the absolute value of optical constants: such data will lead to a better understanding of core-orthogonalization and local field effects in semiconductors.

Finally, the techniques we have applied in this paper or identified for future study could be extended to a wide variety of semiconductors. Such efforts might lead to a better understanding of the role of ionicity in determining the range of validity of the independent-particle model in these materials, and will lead to a deeper understanding of chemical trends and physical properties of semiconductors.

ACKNOWLEDGMENTS

We wish to thank M. Erbudak, who participated in the data collection process.

We acknowledge useful conversations with D. Aspnes, J. Chelikowski, Marvin L. Cohen, T. Donovan, J. Janak, E. O. Kane, V. Moruzzi, J. C. Phillips, W. L. Schaich, J. Shaw, W. E. Spicer, F. Stern, J. Van Vechten, and A. Williams.

APPENDIX: DETAILS OF ANISOTROPIC DIRECT-TRANSITION MODEL AND COMPARISON OF ITS PREDICTIONS WITH EXPERIMENT

This appendix presents a more detailed description of certain aspects of the direct-transition model for photoemission described by Eqs. (3.8)–(3.16). These include a description of the way in which Eq. (3.8) is reduced to an integral over $\frac{1}{48}$ of the BZ, a discussion of the transmission function (3.14), modification of the model to describe angle-resolved photoemission, and the justification for not considering in our model the polarization of the synchrotron-radiation uv light used in the experiment or the angular acceptance of the energy analyzer. We also present a comparison of experiment with the present theory and the usual "three-step model."

A. Reduction of integration to $\frac{1}{48}$ th of a BZ

The $\vec{k}$-space integral in Eq. (3.8) can be written in the form

$$I_{nn'}(E_i, h\nu) = \int d^3k f_1(\vec{k}) f_2(\vec{\nabla}_{\vec{k}} E_{n'} \cdot \hat{n}) \times \sum_{\vec{G}} f_3((\vec{k}+\vec{G}) \cdot \hat{n}) , \tag{A1}$$

where

$$f_1 = |P_{nn'}(\vec{k})|^2 \delta(E_n(\vec{k}) - E_i) \delta(E_{n'}(\vec{k}) - E_i - h\nu) , \tag{A2}$$

$$f_2 = D_{n'}(\vec{k}, \hat{n}) , \tag{A3}$$

and

$$f_3 = |C^{n'}_{\vec{G}\vec{k}}|^2 t^{n'}_{\vec{G},\vec{k}} . \tag{A4}$$

The integral has been written in this form to display explicitly the dependence of various factors in the integrand in (3.8) on vector arguments. We can then transform $I_{nn'}$ to an integral over $\frac{1}{48}$ of the BZ as follows:

$$I_{nn'}(E_i, h\nu) = \sum_{\gamma} \int_{(1/48)\,\mathrm{BZ}} d^3k f_1(\gamma\vec{k}) \times f_2(\gamma\vec{\nabla}_{\vec{k}} E_{n'} \cdot \hat{n}) \sum_{G} f_3((\gamma\vec{k}+\vec{G}) \cdot \hat{n}) , \tag{A5}$$

where the γ are 48 matrices which generate all $\vec{k}$ from those contained within the first 48th of the BZ.

We now write

$$f_1(\gamma\vec{k}) = f_1(\vec{k}) ,$$

$$f_2(\gamma\vec{\nabla}_{\vec{k}} E_{n'} \cdot \hat{n}) = f_2(\vec{\nabla}_{\vec{k}} E_{n'} \cdot \gamma^{-1}\hat{n}) ,$$

and

$$\sum_{\vec{G}} f_3((\gamma\vec{k}+\vec{G}) \cdot \hat{n}) = \sum_{\vec{G}} f_3((\gamma\vec{k}+\gamma\vec{G}) \cdot \hat{n}) = \sum_{\vec{G}} f_3((\vec{k}+\vec{G}) \cdot \gamma^{-1}\hat{n}) ,$$

where we have used the invariance of the functions of $\vec{k}$ in (3.8) under symmetry operations of the reciprocal lattice, the invariance of products of the form $\gamma\vec{k} \cdot \hat{n}$ under the transformation of $\vec{k} \cdot \gamma^{-1}\hat{n}$, and the equivalence of any sum over *all* reciprocal-lattice vectors $\vec{G}$ under the replacement $\vec{G} \to \gamma\vec{G}$ for *any* γ.

Thus (A5) becomes

$$I_{nn'}(E_i, h\nu) = \sum_{\gamma} \int_{(1/48)\,\mathrm{BZ}} d^3k f_1(\vec{k}) \times f_2(\vec{\nabla}_{\vec{k}} E_{n'} \cdot \gamma^{-1}\hat{n}) \sum_{\vec{G}} f_3((\vec{k}+\vec{G}) \cdot \gamma^{-1}\hat{n}) . \tag{A6}$$

The set of 48 γ^{-1} operating on the crystal-surface normal $\hat{n}$ generates all equivalent surface normals $\hat{n}_i$, each of them being generated $48/N_{\hat{n}}$ times, where $N_{\hat{n}}$ is the number of surface normals equivalent to $\hat{n}$ under the operations of the full symmetry group for the cubic lattice. We can then finally rewrite (A1) as

$$I_{nn'}(E_i, h\nu) = \frac{48}{N_{\hat{n}}} \sum_{\hat{n}_i} \int_{(1/48)\,\mathrm{BZ}} d^3k f_1 f_2 \sum_{G} f_3 . \tag{A7}$$

The meaning of (A7) is that the $\vec{k}$-space integration over all $\vec{k}$ in (3.8), which describes photoemission through *one* surface with normal $\hat{n}$, can be replaced by the sum (over emission through all sur-

faces $\hat{n}_i$ equivalent to $\hat{n}$) of the integral over one $\frac{1}{48}$ of the BZ. For cleaved Ge, $\hat{n}$ is in the (111) direction, and one should sum (A7) over all equivalent $\langle 111\rangle$ directions (i.e., $N_{\hat{n}}=8$). In practice, the sum over $\hat{n}_i$ in (A7) can be brought inside the integrand and applied to the few factors which contain $\hat{n}$, so that one first sums and then performs a single $\vec{k}$-space integration.

B. Surface transmission probability and angle-resolved photoemission

We start with a Bloch wave expanded in a plane-wave basis set [Eq. (3.13)] and a surface potential barrier of the form $f(\vec{r})=f(z)$ [Eq. (3.12)], where z is the direction normal to the surface. That is, we assume that the weak pseudopotential *along* the surface does not mix the plane-wave components of $\psi_{n'\vec{k}}$ in (3.13) in any significantly different way than does the bulk crystal Hamiltonian.

The plane-wave components of $\psi_{n'k'}$, $e^{i(\vec{k}+\vec{G}_i)\cdot\vec{r}} \equiv |\vec{k}+\vec{G}_i\rangle$, then match to waves $|\vec{K}_i\rangle$ outside the solid such that momentum parallel to the surface and energy are conserved; i.e., we require that

$$E_{n'}(\vec{k}) - V_0 = \hbar^2 K_i^2/2m \quad \text{for all } i \tag{A8}$$

and

$$(\vec{K}_i)_{\parallel} = (\vec{k}+\vec{G}_i)_{\parallel} \, . \tag{A9}$$

Thus the normal component of energy of plane wave $\vec{K}_i$ outside the solid is

$$\begin{aligned} E_{\perp}^{(i)} &= \hbar^2[K_i^2 - (\vec{K}_i)_{\parallel}^2]/2m \\ &= E_{n'}(\vec{k}) - V_0 - \hbar^2(\vec{k}+\vec{G}_i)_{\parallel}^2/2m \, . \end{aligned} \tag{A10}$$

A necessary condition for transmission of a plane-wave component is that $E^{(i)}$ must exceed the barrier height. However, in the case that $E^{(i)} > V_0$ but $(E_{\perp}^{(i)} - V_0)/V_0 \ll 1$, the quantum-mechanical transmission coefficient $t_{\vec{G}_i,\vec{k}}^{n'}$ in Eq. (3.14) should be less than 1. The worse case is if the surface potential barrier is a step potential [see Fig. 18(a)], in which case $t_{\vec{G}_i,\vec{k}}^{n'}$ is smallest for a given value of $(E_{\perp}^{(i)} - V_0)/V_0$ [Fig. 18(b), curve 1]. The actual barrier in a real solid looks more like the dashed curve in Fig. 18(a), and for this barrier the quantum-mechanical transmission function [curve 2 in Fig. 18(b)] approaches the classical one [curve 3 in Fig. 18(b)]. From Fig. 18(b) we see that the classical transmission function we use in our anisotropic model, Eq. (3.14), is an excellent approximation. We have tested this approximation by calculating spectra with the two extreme transmission functions, represented by curves 1 and 3 in Fig. 18(b). The difference was slight, giving a small reduction in amplitude of the calculated spectra for the first few eV above threshold. For these reasons we choose the more realistic, classical extreme, curve 3 in Fig. 18(b), which is closest to the true situation (curve 2). We note that choosing curve 3 (or 2) will produce the observed $(h\nu - h\nu_{\text{threshold}})^2$ dependence of the quantum yield $Y(h\nu)$ near threshold (Fowler law[25]), while the quantum-mechanical transmission for the potential step [curve 1 of Fig. 18(b)] would predict a (unobserved) deviation from this law.

At this point we discuss the use of a sum of transmission probabilities for individual plane-wave components of $\psi_{n'\vec{k}}$ in Eq. (3.15) for the total transmission rather than a sum of amplitudes, squared. The reason for this form, even though the various transmitted waves are coherent, is that the excited Bloch wave is actually localized in space, so that for any detector at a large distance from the sample the individual beams diverge and do not overlap (or interfere) by the time they reach the detector. This is similar to the case of LEED, where coherently backscattered "plane-wave" beams cause a spot pattern on a LEED screen rather than an interference pattern.

These ideas result in a simple change in the anisotropic direct-transition model in order to describe angle-resolved photoemission. In this case, we select only those beams which are directed toward the angular region of acceptance of the detector. More generally, if $\overline{T}(\theta, \phi)$ is the transmission function of the energy analyzer, then we replace Eq. (3.15) by

$$T_{n'}(\vec{k}, \hat{n}) = \sum_i t_{\vec{G}_i,\vec{k}}^{n'} \left| C_{\vec{G}_i,\vec{k}}^{n'} \right|^2 T(\theta_i, \phi_i) \, , \tag{A11}$$

where θ_i and ϕ_i are determined by Eqs. (A8) and (A9) (with $\hat{n}\cdot\vec{r}>0$):

$$\sin\theta_i = \frac{(\vec{k}+\vec{G}_i)_{\parallel}}{\{2m[E_{n'}(\vec{k}) - V_0]/\hbar^2\}^{1/2}}$$

and

$$\cos\phi_i = (\vec{k}+\vec{G}_i)_{\parallel} \cdot \hat{\beta}/\left|(\vec{k}+\vec{G}_i)_{\parallel}\right| \, , \tag{A12}$$

where $\hat{\beta}$ is a unit vector in the plane of the surface which defines $\phi = 0$.

C. Comparison with experiment

We end by addressing the two questions: (i) What is the justification for ignoring the synchrotron light polarization, and the angular acceptance of the energy analyzer, in comparing theory with experiment? (ii) How well do the predictions of the anisotropic direct-transition model compare with experiment?

The calculations we perform are for unpolarized light [$\hat{\epsilon}\cdot\vec{p}$ does not appear[24] in the matrix elements $P_{nn'}$ in Eq. (3.8) where $\hat{\epsilon}$ is light polarization and $\vec{p}$ the momentum operator]. Also, we have assumed collection of all electrons leaving the sample [we use Eq. (3.15) rather than (A11) to describe the transmission function]. However, our

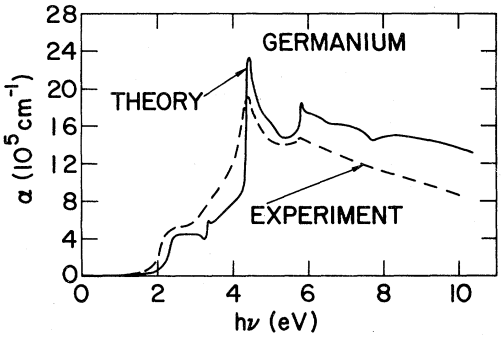

FIG. 19. Theoretical absorption coefficient $\alpha(h\nu)$, obtained using $\epsilon_2(h\nu)$ in Fig. 10 and a Kramers–Kronig analysis (solid line), is compared with the experimental $\alpha(h\nu)$ described in Ref. 80 (dashed).

data were obtained in a spectrometer (see Ref. 28) in which polarized synchrotron-radiation light and a cylindrical-mirror electron energy analyzer (CMA) were used. The CMA axis was at a large angle (~ 35°) with respect to the sample normal, so electrons with a wide range of polar and azimuthal angles were collected. Even more important, we found that spectra obtained by Donovan[31] below 11.6 eV (LiF window cutoff) using unpolarized light normal to a (111) cleaved surface, and collecting all emitted electrons, were essentially identical to ours.

Also, in the geometry of our experiment, the light was always polarized in the plane of the surface, as for Donovan's experiment, but we only had one of the two orthogonal polarizations obtained in Donovan's experiment. Thus one avoided surface-electric-field-enhancement effects of the

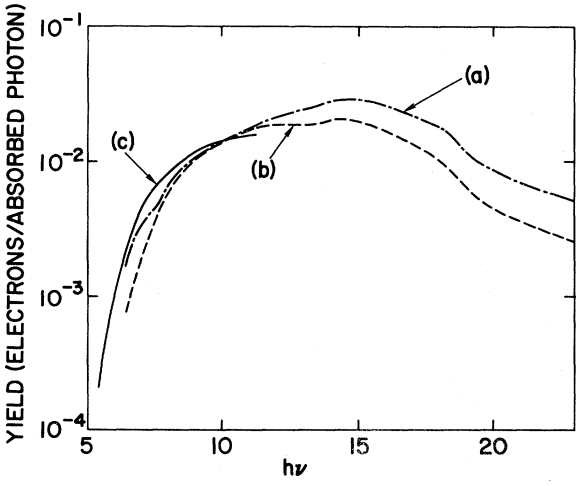

FIG. 20. (a) Theoretical quantum yield $Y(h\nu)$ for the Fig. 9 energy bands and the anisotropic direct-transition model. (b) Theoretical $Y(h\nu)$ using the isotropic model. (c) Experimental yield from Ref. 31. Curves (a) and (b) were normalized to (c) at 10 eV.

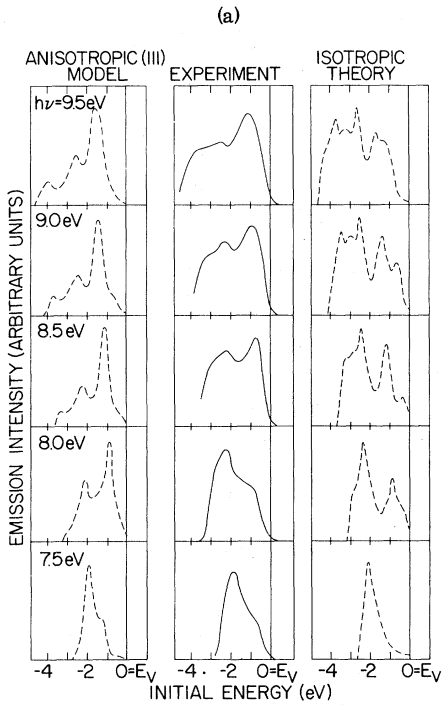

FIG. 21. (a) Comparison of experimental PED's with theory for $7.5 \leq h\nu \leq 9.5$ eV using two theoretical photoemission models and the energy bands shown in Ref. 19 (obtained using potential III of Table I). (b) Comparison of theory and experiment for $10 \leq h\nu \leq 14$ eV.

type discussed by Kliewer.[7] However, it is possible that certain intensity differences for some spectral

features (see Figs. 3 and 4, obtained with different samples) are due to the different orientations of the samples with respect to $\hat{\epsilon}$. Alternatively, different cleave qualities might account for the difference.

Finally, we compare the anisotropic direct-transition model for Sec. III with the usual[22-25] isotropic "three-step model." We present here a more detailed comparison of experiment and theory than is given in Refs. 19–21. For example, we first calculate the quantum yield, starting with a determination of $\epsilon_2(h\nu)$ obtained using energy bands and wave functions of potential I of Table I as discussed in Sec. V. From these we obtained the optical absorption coefficient $\alpha(h\nu)$ which appears in Eq. (3.11) of the anisotropic model and in a corresponding equation in the isotropic model.[24] Figure 19 compares our calculated $\alpha(h\nu)$ with that measured by Phillip and Taft.[79] With α obtained theoretically, we were able to calculate $Y(h\nu)$ using both the isotropic and anisotropic theoretical models. The results are compared with experiment in Fig. 20, and we see that the anisotropic model fits experiment better, being higher in the 5–10-eV region than is the yield calculated using the isotropic theory. Evidentally the anisotropic theory's relative enhancement of states which match through the (111) surface is a correction in the right direction to achieve better agreement with experiment. In producing Fig. 21, $Y(h\nu)$ for both theoretical models was normalized to the experiment at $h\nu = 10$ eV. This normalization represents the one adjustable parameter in the theory, which represents an unknown electron-electron scattering matrix element in the Kane random-$\vec{k}$ theory describing secondary electron production.[24,44]

Finally, we calculate photoemission spectra for both theoretical models using energy bands obtained from pseudopotential III of Table I, and compare the calculated spectra with experiment for nine photon energies in the range $7.5 \leq h\nu \leq 14$ eV. The results are shown in Fig. 21, and represent a more complete demonstration of the effects described in Refs. 19–21, namely that the anisotropic model gives a better account of which transitions (permitted by energy and $\vec{k}$ conservation) produce final-state electrons which have a high probability of being photoemitted.

---

*Work supported in part by the NSF under Grant No. GH-35823, the AFOSR under Contract No. F44620-70-C-0089, and the AEC under Contract No. AT(11-1)3063.

[1]J. C. Phillips, Solid State Phys. 16, (1965).
[2]F. Herman *et al.*, in *Methods in Computational Physics*, edited by B. Alder, S. Fernbach, and M. Rotenberg (Academic, New York, 1968), Vol. 8, pp. 193–250.
[3]M. Cardona, Solid State Phys. Suppl. 11, (1969).
[4]Marvin L. Cohen and V. Heine, Solid State Phys. 24, 38 (1970).
[5]P. J. Feibelman and D. E. Eastman, Phys. Rev. B 10, 4932 (1974).
[6]However, in the case where the initial state is a core level whose binding energy has ben determined using photoemission, optical spectroscopy is becoming increasingly useful for identifying conduction-band features (Refs. 7 and 8).
[7]F. C. Brown and O. P. Rustgi, Phys. Rev. Lett. 28, 497 (1972).
[8]D. E. Aspnes and C. G. Olson, Phys. Rev. Lett. 34, 1605 (1974).
[9]F. G. Allen and G. W. Gobeli, J. Appl. Phys. 35, 597 (1964); Phys. Rev. 144, 558 (1966).
[10]T. M. Donovan, Stanford Electronics Laboratories, Stanford University, Technical Report No. 5221-2 (unpublished).
[11]W. E. Spicer, J. Phys. (Paris) 34, C6-19 (1973).
[12]W. D. Grobman and D. E. Eastman, Phys. Rev. Lett. 29, 1508 (1972).
[13]D. E. Eastman *et al.*, Phys. Rev. 9, 3473 (1974), and references therein.
[14]D. E. Eastman, in *Proceedings of the IV International Conference on Vacuum uv Physics* (Pergamon, Hamburg, 1974), p. 417 ff.
[15]J. E. Rowe and H. Ibach, Phys. Rev. Lett. 31, 102 (1973).
[16]N. J. Shevchik *et al.*, J. Phys. (Paris) 34, C6-45 (1973).
[17]R. A. Pollak *et al.*, Phys. Rev. Lett. 29, 1103 (1972); L. Ley *et al.*, Phys. Rev. B 9, 600 (1974).
[18]D. E. Eastman, J. L. Freeouf, and M. Erbudak, AIP Conf. Proc. 20, 95 (1974); see also Ref. 29.
[19]W. D. Grobman *et al.*, in *Proceedings of the XII International Conference on the Physics of Semiconductors, Stuttgart*, 1974 (Teubner, Stuttgart, 1974), pp. 1275–1284.
[20]W. D. Grobman and D. E. Eastman, Phys. Rev. Lett. 33, 1034 (1974).
[21]W. D. Grobman, Comments Solid State Phys. (to be published).
[22]C. N. Berglund and W. E. Spicer, Phys. Rev. 136, A1030 (1964); 136, A1044 (1964); also, see Ref. 7 of Ref. 14 above.
[23]J. Janak *et al.*, in *Electronic Density of States*, edited by L. H. Bennett, Natl. Bur. Stand. (U.S.) Spec. Publ. 323 (U.S. GPO, Washington, D.C., 1971), p. 181; J. Janak, in *Computational Methods in Band Theory*, edited by P. M. Marcus *et al.* (Plenum, New York, 1971), p. 323.
[24]J. F. Janak, A. R. Williams, and V. L. Moruzzi, Phys. Rev. B 11, 1522 (1975).
[25]D. E. Eastman, in *Techniques of Metals Research VI*, edited by E. Passaglia (Interscience, New York, 1972), pp. 413–479; W. D. Grobman and D. E. Eastman, Surf. Sci. 37, 355 (1973).
[26]N. V. Smith, Crit. Rev. Solid State Sci. 2, 45 (1971).
[27]A detailed description of this apparatus, including sample preparation techniques, resolution, count rates, etc., appears in Ref. 13.
[28]See Ref. 13. We note that through a typographical error L_1 in Table I is listed as -7.4 eV, which should be changed to -7.7 eV as in Ref. 12.
[29]D. E. Eastman and J. L. Freeouf, Phys. Rev. Lett. 33, 1601 (1974); also see Ref. 18.
[30]W. Gudat and C. Kunz, Phys. Rev. Lett. 29, 169 (1972).

[31]T. M. Donovan, Ph. D. thesis (Stanford University) (unpublished).
[32]G. W. Gobeli and F. G. Allen, Phys. Rev. 127, 141 (1962); L. F. Wagner and W. E. Spicer, Phys. Rev. B 9, 1512 (1974).
[33]D. Jepsen, P. Marcus, A. Ignatiev, and F. Jona (unpublished).
[34]C. J. Powell, Surf. Sci. 44, 29 (1974).
[35]A similar approximation, as well as a figure similar to Fig. 5, appears in Ref. 5. We use a slightly different model for $n(E)$ and k_{BZ} and have specialized the figure to the case of Si and Ge.
[36]In the case that escape depths are so short that only the amplitude of the bulk wave function in the surface layer is relevant, one may see extreme distortions due to a strong variation of bulk band charge in the surface layer with energy. Such a strong variation, for certain bands, has been predicted, for example, by J. A. Appelbaum and D. R. Hamann, Phys. Rev. B (to be published).
[37]K. C. Pandey and J. C. Phillips, Phys. Rev. B 9, 1552 (1974).
[38]J. C. Phillips and K. C. Pandey, Phys. Rev. Lett. 30, 787 (1973).
[39]One theory of this effect is given by L. Hedin and B. I. Lundqvist, J. Phys. C 4, 2064 (1971).
[40]M. L. Cohen and T. K. Bergstresser, Phys. Rev. 141, 789 (1966).
[41]V. Heine and I. Abarenkov, Philos. Mag. 9, 451 (1964).
[42]J. R. Chelikowsky and M. L. Cohen, Phys. Rev. Lett. 31, 1582 (1973).
[43]J. R. Chelikowsky, D. J. Chadi, and Marvin L. Cohen, Phys. Rev. B 8, 2786 (1973).
[44]E. O. Kane, Phys. Rev. 159, 624 (1967).
[45]G. Gilat and L. J. Raubenheimer, Phys. Rev. 144, 390 (1966).
[46]D. Brust [Phys. Rev. 139, A489 (1965)] and L. R. Saravia and L. Casamayou [J. Phys. Chem. Solids 32, 1541 (1971)] have attempted analyses of BZ volume contributions to photoemission spectra. Their final results were incorrect because of the lack of accurate starting-band calculations, the fact that data over a limited energy range were then available, and the use of an oversimplified, isotropic model.
[47]D. E. Eastman and W. D. Grobman, Phys. Rev. Lett. 28, 1378 (1972).
[48]W. D. Grobman and D. E. Eastman, Phys. Rev. Lett. 29, 1508 (1972).
[49]F. C. Brown and O. P. Rustgi, Phys. Rev. Lett. 28, 497 (1972).
[50]W. E. Spicer, J. Phys. (Paris) 34, C6-19 (1973).
[51]J. Matsuzaki, Stanford Electronics Laboratory, Stanford University, Report No. 5220-3 (unpublished).
[52]L. R. Saravia and L. Casamayou, J. Phys. Chem. Solids 33, 145 (1972).
[53]H. R. Philipp and H. Ehrenreich, Phys. Rev. 129, 1550 (1963).
[54]R. R. L. Zucca and Y. R. Shen, Phys. Rev. B 1, 2668 (1970).
[55]G. G. Macfarlane *et al.*, Phys. Rev. 108, 1377 (1957); 111, 1245 (1958).
[56]G. J. Lapeyre *et al.*, Phys. Rev. Lett. 33, 1290 (1974).
[57]See p. 16 of Ref. 31.
[58]E. O. Kane, Phys. Rev. 175, 1039 (1968).
[59]J. R. Chelikowsky and Marvin L. Cohen (private communication).
[60]Other calculations of $R(h\nu)$, for several different semiconductors, are compared with the experimental results of Philipp and Ehrenreich (Ref. 53) in Ref. 4. In all cases theory predicts results for $R(h\nu)$ about twice as large as experiment for $h\nu \gtrsim 10$ eV, but rather good agreement below ~ 6 eV. The experimental reflectance amplitude is thus possibly wrong, although the discrepancy could also be due in part to local-field effects.
[61]D. E. Aspnes, Phys. Rev. Lett. 31, 230 (1973).
[62]J. R. Chelikowsky and Marvin L. Cohen, Phys. Rev. Lett. 33, 1339 (1974).
[63]W. A. Harrison, *Pseudopotentials in the Theory of Metals* (Benjamin, New York, 1966), Sec. I-3.
[64]J. P. Walter and M. L. Cohen, Phys. Rev. B 4, 1877 (1971).
[65]E. O. Kane, in *Proceedings of the XI International Conference on the Physics of Semiconductors, Stuttgart*, 1974 (Teubner, Stuttgart, 1974), p. 169, and Refs. therein. Also, E. O. Kane [Phys. Rev. B 4, 1917 (1971)] found that, owing to the different charge localization in conduction and valence states, exchange corrections to states below and above the fundamental gap are quite different in magnitude.
[66]K. Zeppenfeld and H. Raether, Z. Phys. 193, 471 (1966).
[67]It is possible that a feature near 8 eV in the thermoreflectance spectrum of Ge [G. Guizzeti *et al.*, Phys. Rev. B 9, 640 (1974)] is related to this transition.
[68]P. Wolff, Phys. Rev. 92, 18 (1953).
[69]H. Frölich and H. Pelzer, Proc. Phys. Soc. Lond. A 68, 525 (1955).
[70]H. Ehrenreich and M. H. Cohen, Phys. Rev. 115, 786 (1959).
[71]J. A. Van Vechten, Phys. Rev. 182, 891 (1969).
[72]See Ref. 71 and J. C. Phillips, Rev. Mod. Phys. 42, 317 (1970).
[73]B. Feuerbacher *et al.*, J. Opt. Soc. Am. 58, 1434 (1968).
[74]J. A. Appelbaum, Phys. Rev. 144, 435 (1966); J. P. Van Dyke [Phys. Rev. B 5, 1489 (1972)] has done a theoretical calculation for Ge in which he concludes that core orthogonalization effects are too small to explain the intensity difference.
[75]J. A. Van Vechten and R. M. Martin, Phys. Rev. Lett. 28, 446 (1972); 28, 646(E) (1972); T. K. Bergstresser and G. W. Rubloff, Phys. Rev. Lett. 30, 794 (1973); W. R. Hanke and L. J. Sham, Phys. Rev. Lett. 33, 582 (1974); S. G. Louie, J. R. Chelikowsky, and M. L. Cohen, Phys. Rev. Lett. 34, 155 (1975).
[76]N. V. Smith and M. M. Traum [Phys. Rev. Lett. 31, 1247 (1973)] obtained angle-resolved spectra for cleaved (110) GaAs which also showed some conservation of crystal momentum in the photoemission process at low $h\nu$. However, experimental results on emission from different faces of single-crystal Ag and Cu were not well described by simplified anisotropic models owing probably to the different specular/diffuse nature of a metal surface compared to that on a cleaved semiconductor. See P. O. Nilsson and D. E. Eastman, Phys. Scr. 8, 113 (1973); J. E. Rowe and N. V. Smith, Phys. Rev. B 10, 3207 (1974). Other angle-resolved photoemission experiments have also been used to obtain band-structure information, including the work reported by U. Gerhardt and E. Dietz, Phys. Rev.

Lett. 26, 1477 (1971); T. Gustafsson, P. O. Nilsson, and L. Wallden, Phys. Lett. A 37, 121 (1971); R. Y. Koyama and L. R. Hughey, Phys. Rev. Lett. 29, 1518 (1972); R. H. Williams, J. M. Thomas, M. Barber, and N. Alford, Chem. Phys. Lett. 17, 142 (1972); I. Lindau and S. B. M. Hagström, J. Phys. E 4, 936 (1971); R. T. Poole, R. C. G. Leckey, J. G. Jenkin, and J. Liesegang, J. Electron Spectrosc. 1, 371 (1973).

[77]D. E. Aspnes, Phys. Rev. B (to be published); also, see Ref. 8.

[78]K. L. Kliewer, Phys. Rev. Lett. 33, 900 (1974).

[79]H. R. Philipp and E. A. Taft, Phys. Rev. 113, 1002 (1959).